New Postprocessing Methods for Remote Sensing Image Classification: A Systematic Study

Xin Huang, *Member, IEEE*, Qikai Lu, Liangpei Zhang, *Senior Member, IEEE*, and Antonio Plaza, *Senior Member, IEEE*

***Abstract*—This paper develops several new strategies for remote sensing image classification postprocessing (CPP) and conducts a systematic study in this area. CPP is defined as a refinement of the labeling in a classified image in order to enhance its original classification accuracy. The current mainstream classification methods (preprocessing) extract additional spatial features in order to complement spectral information and enhance classification using spectral responses alone. On the other hand, however, the CPP methods, providing a new solution to improve classification accuracy by refining the initial result, have not received sufficient attention. They have potential for achieving comparable accuracy to the preprocessing methods but in a more direct and succinct way. In this paper, we consider four groups of CPP strategies: 1) filtering; 2) random field; 3) object-based voting; and 4) relearning. In addition to the state-of-the-art CPP algorithms, we also propose a series of new ones, e.g., anisotropic probability diffusion and primitive cooccurrence matrix. In experiments, a number of multisource remote sensing data sets are used for evaluation of the considered CPP algorithms. It is shown that all the CPP strategies are capable of providing more accurate results than the raw classification. Among them, the relearning approaches achieve the best results. In addition, our relearning algorithms are compared with the state-of-the-art spectral–spatial classification. The results obtained further verify the effectiveness of CPP in different remote sensing applications.**

***Index Terms*—Anisotropic diffusion, classification, cooccurrence matrix (PCM), filtering, Markov random field (MRF), object-based, postprocessing, reclassification, relearning.**

I. Introduction

CLASSIFICATION, as a classical and basic problem in many remote sensing disciplines, has been extensively studied. It provides a set of elementary input parameters for various remote sensing applications, such as land-cover/use mapping, change detection, environmental assessment, and landscape analysis. Traditional classification algorithms use pixelwise methods with only spectral information considered, such as maximum-likelihood classification [1], spectral unmixing [2], decision tree [3], more advanced hybrid classification [4], support vector machines [5], or the artificial immune network classifier [6], among several others. These methods were constructed based on medium or low spatial resolution images where a large number of mixed pixels exist, and radiometric signals are the most important information source for image interpretation. In pace with the increasing availability of high spatial resolution images, the traditional per-pixel classification methods have been proved to be inadequate for information extraction because the spectral information alone fails to model the complicated and detailed geospatial structures in the high-resolution data [7]. In this context, researchers have proposed to exploit the spatial features as a complementary source of information to the spectral bands. As a result, many spectral–spatial classification techniques have been developed in order to enhance the accuracy of the traditional classification approaches [8].

The most commonly used spatial features for classification purposes include wavelet textures [9], gray-level cooccurrence matrix (GLCM) [10], pixel shape index [5], and morphological profiles [11]. Meanwhile, in recent years, object-based image analysis (OBIA) has received much interest. The basic idea of OBIA is to segment the spatially adjacent pixels into spectrally similar objects and then conduct image analysis on the objects as the minimum unit of information [12]. OBIA has been successfully applied to mapping private gardens [13], urban tree species [14], forests [15], and urban shadow [16].

The aforementioned spatial feature extraction strategies can be viewed as a form of preprocessing prior to classification, which generates a series of additional features from the original images, in order to improve the classification accuracy that can be obtained in the original spectral space. However, classification postprocessing (CPP) has not received sufficient attention. We define CPP as *a refinement of the labeling in a classified image in order to enhance its original classification accuracy*. The basic assumption is that adjacent pixels are more likely to belong to the same class, i.e., things that are near tend to be more related between them than those that are distant.

The simplest CPP method is the majority filter [17]. Here, a moving window is centered at each pixel in a classified image, and the class that appears more often in the window is then assigned to the central pixel. Schindler [18] proposed to use Gaussian smoothing, bilateral filtering, and an edge-aware filter for postclassification smoothing. These advanced filtering algorithms consider the probabilistic outputs of the classifier

Manuscript received October 11, 2013; revised January 6, 2014 and February 14, 2014; accepted February 18, 2014. Date of publication March 17, 2014; date of current version May 30, 2014. This work was supported in part by the National Natural Science Foundation of China under Grant 41101336 and Grant 91338111, by the Program for New Century Excellent Talents in University of China under Grant NCET-11-0396, and by the Foundation for the Author of National Excellent Doctoral Dissertation of PR China (FANEDD) under Grant 201348.

X. Huang, Q. Lu, and L. Zhang are with the State Key Laboratory of Information Engineering in Surveying, Mapping and Remote Sensing, Wuhan University, Wuhan 430079, China (e-mail: huang_whu@163.com).

A. Plaza is with the Department of Technology of Computers and Communications, University of Extremadura, 10003 Cáceres, Spain (e-mail: aplaza@unex.es).

Color versions of one or more of the figures in this paper are available online at http://ieeexplore.ieee.org.

Digital Object Identifier 10.1109/TGRS.2014.2308192

TABLE I
CPP ALGORITHMS USED IN THIS STUDY (THE NEWLY PROPOSED ALGORITHMS ARE HIGHLIGHTED IN BLUE)

CPP strategy	Specific algorithms
Filtering	Majority Gaussian Bilateral Edge-aware Anisotropic diffusion
Object-based voting	Crisp voting Soft voting
Random field	MRF
Relearning	Relearning-Hist Relearning-PCM

and impose anisotropic weights on the pixels in the moving window, which is a strategy that leads to better results than the traditional majority filter.

Markov random fields (MRFs) [19] can be viewed as an effective CPP strategy, since they are able to smooth the classification and provide more homogeneous results on the condition that the neighbors with the same label are preferred and those with different labels are panelized. Solaiman *et al.* [20] proposed an information fusion CPP method, where the edge features derived from the original image as well as the thematic map are used to produce classification maps with sharp boundaries and homogeneous regions. In [21], the directional information is imposed on the probabilistic relaxation model for postprocessing, in order to preserve the linear features. Some CPP studies refer to knowledge or rules [8], [22], i.e., a set of rules (e.g., shape, semantics, and context) are defined and implemented on the raw classification results. However, these assumptions or rules are dependent on the specific image scenes and difficult to generalize.

Although some CPP algorithms exist, they have not received due attention in their capacity for enhancing remote sensing image classifications. To the best of our knowledge, a comprehensive evaluation (and further improvement) of techniques for CPP is currently lacking. In this context, we aim to systematically investigate the available CPP methods for remote sensing images and develop new strategies, analyzing their potential for improving the obtained image classification results. As shown in Table I, the CPP algorithms considered in this study are categorized into four groups:

1) *Filtering*: In this group of algorithms, the final decision on the label of the central pixel within a window is determined by considering the class labels and probabilities of all the pixels in the window. In this paper, anisotropic diffusion filtering [23] is adopted for the first time in the CPP problem.
2) *Object-based voting (OBV)*: Majority voting is conducted within each image object, based on an initial pixelwise classification.
3) *Markov random fields (MRFs)*: MRF is able to take advantage (in a flexible manner) of the contextual information associated with images and the dependence among neighboring pixels to improve the raw classification [19].
4) *Relearning*: Relearning is an innovative CPP strategy that we present in this contribution. It aims at iteratively learning the classified image by considering the frequency and spatial arrangement of the class labels. Unlike the three aforementioned kinds of CPP strategies, relearning is effective not only in terms of smoothing the classification result but also in the task of enhancing class separability. In this paper, we propose two novel relearning algorithms. The first one (called relearning-Hist) is based on the class histogram, where the class frequency histogram (calculated for the classified pixels within a moving window) is used as a statistical feature for iterative reclassification. The second one is the primitive cooccurrence matrix (called relearning-PCM), where both the frequency and the spatial arrangement of the classified pixels within a moving window are simultaneously considered.

In order to comprehensively evaluate the performance of the considered CPP algorithms, a series of multisource remote sensing images are considered in the experiments, including hyperspectral (two data sets), high-resolution (three data sets), and SAR images (two data sets). Moreover, a comparative study is conducted between the considered CPP methods and the current mainstream spectral–spatial techniques for remote sensing image classification. The main contributions of this paper can be therefore summarized as follows.

1) We propose a series of novel CPP algorithms (see Table I).
2) We perform a systematic investigation of (available and new) CPP strategies.
3) We conduct a detailed comparison between CPP techniques and several commonly used spectral–spatial classification methods.

The remainder of this study is organized as follows: Section II describes various state-of-the-art CPP algorithms, and Section III focuses on the proposed relearning methods, which are the main contributions of this paper. Section IV introduces the multisource remote sensing data sets used for validation purposes. Section V presents our experimental results, including a detailed parameter analysis and comparison. Section VI concludes this paper with some remarks and hints at plausible future research lines.

II. STATE-OF-THE-ART CPP METHODS

This section introduces the state-of-the-art CPP strategies, including filters, object-based, and MRF methods. Note that a new CPP algorithm based on anisotropic diffusion is also presented.

A. Filtering-Based Methods

Filtering is the most widely used CPP method in state-of-the-art remote sensing image classification. Filtering is carried out based on a sliding window, and the class of the central pixel is determined by considering the labels, probabilities, and intensity values of all the pixels within it. In this paper, majority, Gaussian, bilateral, and edge-aware filters [18] are investigated for smoothing the classification results. Furthermore, we also

propose a novel anisotropic diffusion CPP filtering. The decision rule of the filtering-based CPP methods is maximization of the probability function

$$C(x) = \arg\max_{i \in C}(\widetilde{p}_{x,i}) \tag{1}$$

where C represents the labeling space, and $C(x)$ is the final label of the pixel x. $\widetilde{p}_{x,i}$ denotes the probability of pixel x belonging to the class i after filtering. A description of these methods follows.

1) Majority filter: The majority class in the sliding window is assigned to the central pixel.
2) Gaussian filter: The class of the central pixel is determined by using the class probabilities and Gaussian distance weighting within the local window w. The likelihood function of the Gaussian filter can be written as

$$\widetilde{p}_{x,i} = \frac{1}{Z(\sigma)} \sum_{y \in w} p_{y,i} \cdot G_\sigma \left(\|x - y\| \right) \tag{2}$$

where G_σ is the Gaussian function with standard deviation σ, and $Z(\sigma)$ is the sum-to-one normalization term. $p_{y,i}$ denotes the initial probability that a pixel y belongs to the class i, which is obtained by a pixelwise classifier. w represents the window centered by the pixel x.

3) Bilateral filter: The bilateral filter is an enhanced version of the Gaussian filter that simultaneously considers the distance in the spatial domain and the distance in the intensity (range) domain between the current and the central pixel [24]:

$$\widetilde{p}_{x,i} = \frac{1}{Z(\sigma,\gamma)} \sum_{y \in w} p_{y,i} \cdot G_\sigma \left(\|x - y\| \right) \cdot G_\gamma \left(|I(x) - I(y)| \right) \tag{3}$$

where the spatial and the intensity information are respectively modeled by two Gaussian functions, G_σ and G_γ. The intensity image provides an additional constraint on Gaussian smoothing. In this paper, two intensity images are considered, i.e., the class probability and the original image, respectively, which are denoted as the bilateral and edge-aware filter:
Bilateral filter: $G_\gamma(|I(x) - I(y)|) = G_\gamma(|p_{x,i} - p_{y,i}|)$;
Edge-aware filter: $I(x)$ and $I(y)$ denote the original spectral value for pixel x and y, respectively.

This way, CPP smoothing is strong within relatively homogeneous regions, and boundaries can be better preserved since the similarity of the intensity values between neighboring pixels is considered.

4) Anisotropic diffusion: This approach aims to reduce the image noise without blurring important parts of the image content, e.g., edges and details. The fundamental function adopted by anisotropic diffusion [23] is defined as

$$\frac{\partial I}{\partial t} = d^t(x,y)\Delta I + \nabla d \cdot \nabla I \tag{4}$$

where I is the image, and t is the time of evolution, i.e., the iteration number. Δ and ∇ represent the Laplacian and gradient operators, respectively. d is the diffusion coefficient, which controls the rate of diffusion. A discrete solution of (4) can be derived using the forward-time central-space method:

$$I^{t+1}(x,y) = I^t(x,y) + \lambda \sum_{y \in N_x} d^t(x,y) \cdot \nabla I^t(x,y) \tag{5}$$

where N_x denotes the neighborhood around the central pixel x (4-neighborhood is used for anisotropic diffusion). λ is a constant parameter, controlling the stability of the solution, and its range [0, 0.25] is suggested in [23]. It is set to 0.1 in this study. The diffusion coefficient (so-called flux function) d is a key parameter of the diffusion. According to [23], two functions are defined:

$$d\left(\|\nabla I\|\right) = e^{-\left(\frac{\|\nabla I\|}{K}\right)^2} \tag{6}$$

$$d\left(\|\nabla I\|\right) = \frac{1}{1 + \left(\frac{\|\nabla I\|}{K}\right)^2} \tag{7}$$

where the free parameter K represents the edge-strength to consider in the diffusion. It can be seen that a large value of K will lead to an isotropic diffusion. Anisotropic diffusion was originally adopted for image denoising. In this paper, (5) is transformed into a CPP smoothing method, by defining

$$\widetilde{p}^{t+1}_{x,i} = \widetilde{p}^{t}_{x,i} + \lambda \sum_{y \in N_x} d\left(\left\|\widetilde{p}^{t}_{x,i} - \widetilde{p}^{t}_{y,i}\right\|\right) \cdot \left(\widetilde{p}^{t}_{x,i} - \widetilde{p}^{t}_{y,i}\right),$$

$$\text{with } \widetilde{p}^{t=0}_{x,i} = p_{x,i} \text{ and } \widetilde{p}^{t=0}_{y,i} = p_{y,i}, \tag{8}$$

where the probability image is viewed as the input image I; the gradient ∇ is expressed as the differential image between the central pixel x and its neighborhood N_x. From (8), it can be seen that the class likelihood of each pixel is iteratively updated by considering the similarity of the pixels in a neighborhood. Anisotropic diffusion is an effective approach for image smoothing and denoising, but, surprisingly, it does not seem to have been used for remote sensing image classification purposes.

B. OBV

OBV-based CPP is inspired by the well-known OBIA approach [25]. However, the traditional OBIA method uses the average spectral vector of each object for classification purposes [26]. This strategy does not generally show any improvements over results yielded by using a pixelwise classification based on the spectral information [27]. In this paper, the object-based image processing approach is used for refinement of the raw pixelwise classification, and majority voting is conducted based on the boundary derived from the object-based segmentation.

The quality of image segmentation is a key factor in the performance of the OBIA approach; however, until now, defining the homogeneity criteria and setting the corresponding parameters for the accurate segmentation of remote sensing images has been a difficult problem [28]. In this paper, an adaptive mean-shift segmentation algorithm [12] is utilized for

the OBV. The notable advantage of the adaptive mean-shift lies in the fact that it can automatically choose the spatial bandwidth of the mean-shift procedure according to the characteristics of the local neighborhoods.

OBV is carried out using the label and probability, respectively, for crisp and soft voting:

$$\text{Crisp}: \quad p_{s,i} = \frac{1}{N_s} \sum_{y \in s} \tau\left(C(y) = i\right)$$

$$\text{Soft}: \quad p_{s,i} = \frac{1}{N_s} \sum_{y \in s} p_{y,i} \tag{9}$$

where τ is an indicator function recording the number of times that the pixels within a segment s are classified as class i. N_s is the number of pixels in the segment s. The final label of the segment is determined according to the maximum probability, as indicated in (1).

C. MRF Model

The MRF model is a well-known probabilistic model that is used to integrate the spatial context into image classification problems [19], [29], [30]. It can be regarded as a CPP strategy—note that it fully complies with the definition of a CPP given in this study, i.e., it is able to optimize the raw classification result by imposing the smoothness prior on the pixels. The goal of the MRF is to maximize the global posterior probability, which is equivalent to the minimization of the energy function (i.e., negative log-likelihood) according to Gibbs distribution [19]. A basic expression of the MRF energy can be written as

$$E(X, C) = -\sum_{x \in X} \ln(p_{x,i}) + \beta \sum_{y \in N_x} \left[1 - \delta\left(C(x), C(y)\right)\right] \tag{10}$$

where X and C denote the image and its labeling space, respectively. N_x represents the neighborhood centered by pixel x (8-neighborhood is used for the MRF). $C(x)$ and $C(y)$ are the label of pixel x and y, respectively. $\delta(\cdot)$ is the Kronecker function, i.e., $\delta(x, y) = a$ for $x = y$ and $\delta(x, y) = 0$ otherwise, used to penalize the change of labels in the neighborhood N_x. Here, the constant a can be an arbitrary value since the contribution of the spatial term is controlled by another constant β.

Note that the global minimization of the energy function is NP-hard. Consequently, a key problem for the implementation of MRF is the inference strategy, i.e., how the configuration with minimal energy is found. Traditional optimization techniques use the so-called standard moves, where only one pixel can change its label at a time. The standard moves, however, are a weak condition, frequently leading to low-quality solutions [31]. The iterated conditional modes (ICM) is a well-known method using the standard moves, which chooses the label giving the largest decrease of the energy function until convergence. Another algorithm based on the standard moves is simulated annealing [31], which is easy to implement; however, it requires exponential time for minimization of the energy function. More recently, efficient approximation optimization methods based on graph cuts have been proposed. Specifically, the α-expansion algorithm [31] is used in this study for the optimization of the classical MRF. In contrast to the aforementioned algorithms using standard moves (e.g., ICM and simulated annealing), the expansion algorithm can simultaneously change the labels of arbitrarily large sets of pixels and find a labeling within a known factor of the global minimum [31].

III. Relearning

The aforementioned CPP methods (filtering, OBV, and MRF) are effective for reorganizing and optimizing the raw classification. Nevertheless, they cannot enhance the separability of the classes in the original feature space and, hence, have limited ability for solving the problem of discrimination between spectrally similar classes. Consequently, in this work, we introduce relearning methods based on the distribution of class labels within the neighborhood of each pixel, in order to enhance the separability between similar classes, and then improve the classification results substantially.

A. Relearning-PCM

The first relearning algorithm that we have developed in this contribution is called the primitive cooccurrence matrix (PCM) and is inspired by the well-known GLCM [32]. GLCM is a preprocessing approach that uses the spatial arrangement of the gray level for textural feature extraction [33], whereas PCM is a postprocessing approach in which the spatial arrangement of the class labels is considered for relearning.

Analogous to the GLCM, the basic principle of the PCM is demonstrated in Fig. 1. Its calculation is described in the following steps.

Step 1) The initial classification divides the whole image into C information classes. This step is similar to the quantization step of the GLCM.

Step 2) Based on each moving window (of size $= w$) in the classified image, a $\mathrm{C} \times \mathrm{C}$ PCM is generated, where $\#(\mathrm{C}_i, \mathrm{C}_j)$ represents the number of times that the class i and j occur with distance dis and direction dir. The PCM, therefore, can be expressed as $\mathrm{PCM}(w, dis, dir)$, as shown in Fig. 1.

Step 3) Prior information on the direction for an arbitrary image is often not available. Thus, without loss of generality, the multidirectional PCMs are summed as follows:

$$\mathrm{PCM}(w, dis) = \sum_{dir} \mathrm{PCM}(w, dis, dir) \tag{11}$$

with $dir = (0^\circ, 45^\circ, 90^\circ, 135^\circ)$. Moreover, in this study, only the direct neighbors (i.e., those obtained with $dis = 1$) are considered, and hence, the PCM can be expressed with only one parameter w: $\mathrm{PCM}(w)$. Note that higher-order neighbors might contain additional information for characterizing the spatial correlation between classified pixels (i.e.,

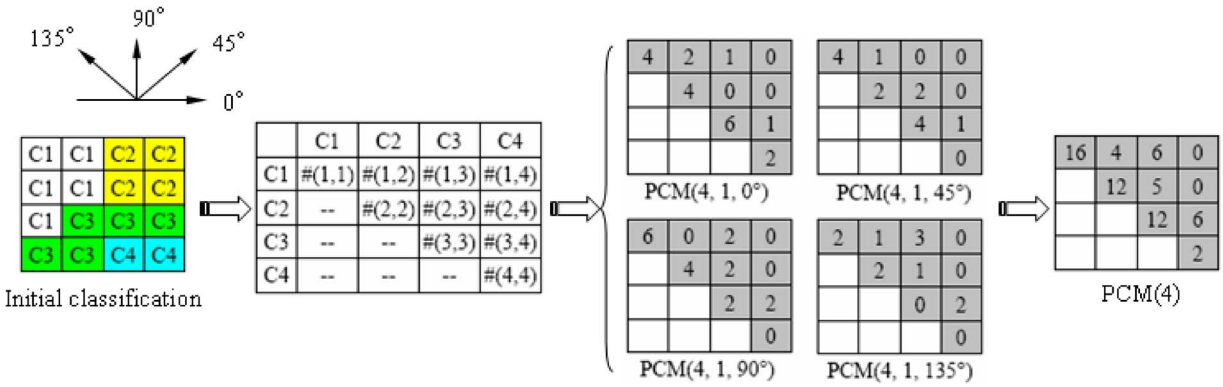

Fig. 1. Demonstration of the PCM.

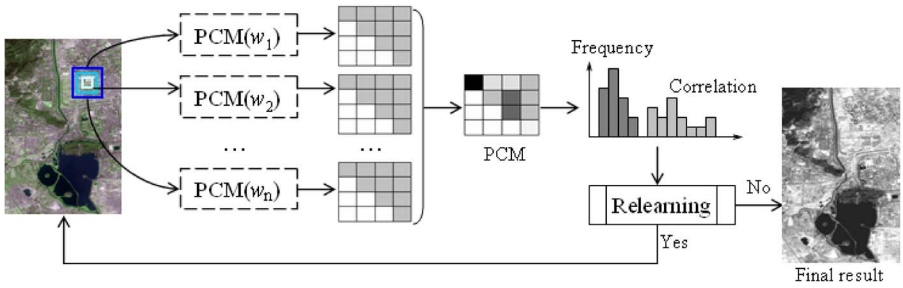

Fig. 2. Flowchart of the relearning-PCM algorithm.

the so-called primitives); however, this complicates the problem and significantly increases the feature dimensionality and computational burden.

Step 4) The primitive matrices derived from the multiple windows can be further integrated because objects in remote sensing imagery generally have multiscale characteristics: $\text{PCM} = \sum_w \text{PCM}(w)$. The final PCM consists of two parts: diagonal elements, which represent the frequency of the primitives in the windows around the central pixel; and nondiagonal elements, which describe the spatial cooccurrence correlation between the classes. Subsequently, the frequency and spatial arrangement of the primitives contained in the PCM are fed into a classifier for relearning, as shown in Fig. 2. Note that relearning is an iterative postclassification method, i.e., the classification is gradually optimized according to the feedback provided by the PCM (class frequency and spatial arrangement). The experiments reported on Section V-B show that only a few iterations are needed to achieve a steady and satisfactory result.

B. Relearning-Hist

The second relearning algorithm developed in this contribution (called relearning-Hist) is based on a local class histogram. The initial classification transforms an image into a new primitive (or labeling) space, based on which the image information can be represented using the occurrence of primitives as a feature vector. It should be noted that the relearning-Hist algorithm concentrates on the frequency of the primitives but not on their spatial arrangement, i.e., only the information on the number

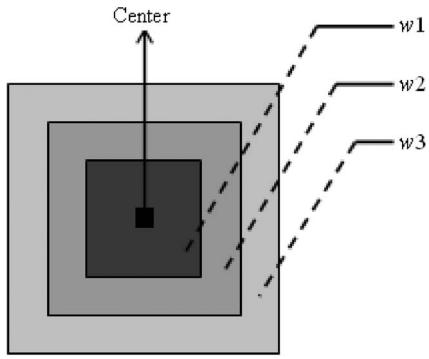

Fig. 3. Weighting kernel for the class histogram.

of occurrences of each primitive is considered. For instance, "a narrow road" and "narrow a road" are regarded as the same by this model. In contrast, the relearning-PCM method takes the order of the primitives into consideration, by which the spatial correlation between neighboring pixels is modeled. This way, "a narrow road" and "narrow a road" represent different configurations. The PCM model, however, only exploits their direct neighbors [$dis = 1$ in (11)] by taking the computational burden into account.

Specifically, the relearning-Hist method is implemented by the following steps:

Step 1) The classes defined in a classified image are viewed as the primitives of an image, providing an implicit representation of the image.

Step 2) Given a moving window w with its central pixel x, the local class histogram (frequency of the primitives) is calculated as follows:

$$\text{hist}(x, w) = \{h_1(x, w), \ldots h_i(x, w), \ldots, h_n(x, w)\} \quad (12)$$

TABLE II
INFORMATION OF THE REMOTE SENSING TEST DATA SETS CONSIDERED IN THIS PAPER

	Sensor	Resolution (m)	Bands	Size	Area
Hyperspectral Datasets	AVIRIS	20	220	145×145	Agriculture
	HYDICE	2.5	191	1280×307	Urban
High spatial resolution datasets	QuickBird	2.4	4	1123×748	Urban
	WorldView-2	2.0	8	600×520	Rural
	ZY-3	5.8	4	651×499	Dense urban
SAR datasets	AirSAR	10.0	36	1024×750	Agriculture
	EMISAR	1.5	42	300×421	Vegetation

where $h_i(x, w)$ denotes the histogram of class i in the local window. In order to consider the multiscale characteristics, in the window, the pixels near the center receive higher weights. As shown in Fig. 3, the window w is divided into three levels, corresponding to different weights, $w1 = 1$, $w2 = 2/3$, and $w3 = 1/3$, respectively, for the calculation of the class histogram. Note that although more sophisticated weighting kernels can be considered, such as the Gaussian kernel, or edge preservation strategies, the multiwindow weighting strategy is adopted in this paper in order to keep consistent with the settings in the PCM algorithm.

Step 3) The class histogram is then used as the input for relearning. The histogram is iteratively updated according to the current classification result, until the relearning stops. The experiments show that we can obtain a steady and accurate classification result after only three iterations.

C. Relation Between Different CPP Methods

The filter-based CPP methods aim to smooth the raw classification, by suppressing the salt-and-pepper effect resulting from the pixelwise processing. Gaussian, bilateral, and edge-aware filters consider distance, probability, and intensity as weighting, respectively, in order to reduce the oversmoothing effect. Moreover, the bilateral filter is a particular choice of weights in an anisotropic diffusion process, which is obtained from geometrical considerations [34], i.e., formally, the bilateral filter is an approximation for the anisotropic diffusion with geometrically sensible weights.

The object-based CPP methods can be cast into the filters. The crisp OBV is actually a majority filter with segmentation-adaptive weights by considering the boundary of each object, and the soft OBV is a probability-based averaging filter with such weights. The OBV-based CPP methods can also be interpreted as smoothness prior, since the pixels within an object are forced to have the same label. As pointed out in [18], however, the main weakness of the OBIA is that the segments cannot precisely delineate the class boundaries. In this context, MRF, which allows one to consider segmentation as a soft constraint, is an appropriate alternative for the crisp segmentation. The MRF-based CPP strategy aims at globally maximizing the posterior probability (or minimizing the energy function) of a classified image. It is also capable of suppressing the pixelwise classification noise (salt-and-pepper) and smoothing the raw result by penalizing the assignment of different labels in the 8-neighborhood.

The relearning CPP methods are different from the aforementioned ones. Their principle is to adaptively learn the spatial arrangement and correlation in a neighborhood of a classified image. The relearning approaches also tend to smooth the raw classification, since in most cases, nearby pixels have the same label. Nevertheless and more importantly, the relearning methods can correct the classification errors (i.e., enhance class separability) by learning the implicit correlation or rules from the spatial arrangement of labels and the class outputs within a neighborhood.

In particular, we would like to emphasize at this point the training approach adopted for the proposed relearning methods. The estimated class patterns by the raw classifier are used as input to the relearning in order to determine the cooccurrence matrix or histograms. The exploitation of the contextual information (e.g., frequency and arrangement of primitives) seems to even out the noise in the initially estimated labeling space. Consequently, all the CPP methods are based on the same amount of information and, hence, can be compared fairly.

IV. DATA AND EXPERIMENTAL SETUP

This section presents the data sets considered and the setup of the parameters used in the experiments.

A. Data sets

In order to test the robustness of the CPP methods discussed in this paper, a series of multisource remote sensing images are adopted, including hyperspectral, high spatial resolution, and SAR data sets. Their basic information is provided in Table II.

1) Hyperspectral Data sets: The AVIRIS image from the Indian Pines test site is a widely used hyperspectral data set in classification applications. The image consists of 145 × 145 pixels, with 220 spectral bands [see Fig. 4(a)], and contains 12 crop types and a total of 10 171 labeled pixels for algorithm testing (Table III). Classification of this image is a very challenging problem because of the strong mixture of the classes' signatures and the unbalanced number of labeled pixels per class [35].

The HYDICE airborne data flight over the Washington DC Mall is also a public hyperspectral data set, which has been widely used for the evaluation of various classification algorithms [36]. Its main characteristic is that it possesses high resolutions in both the spectral and spatial domains (210 narrow

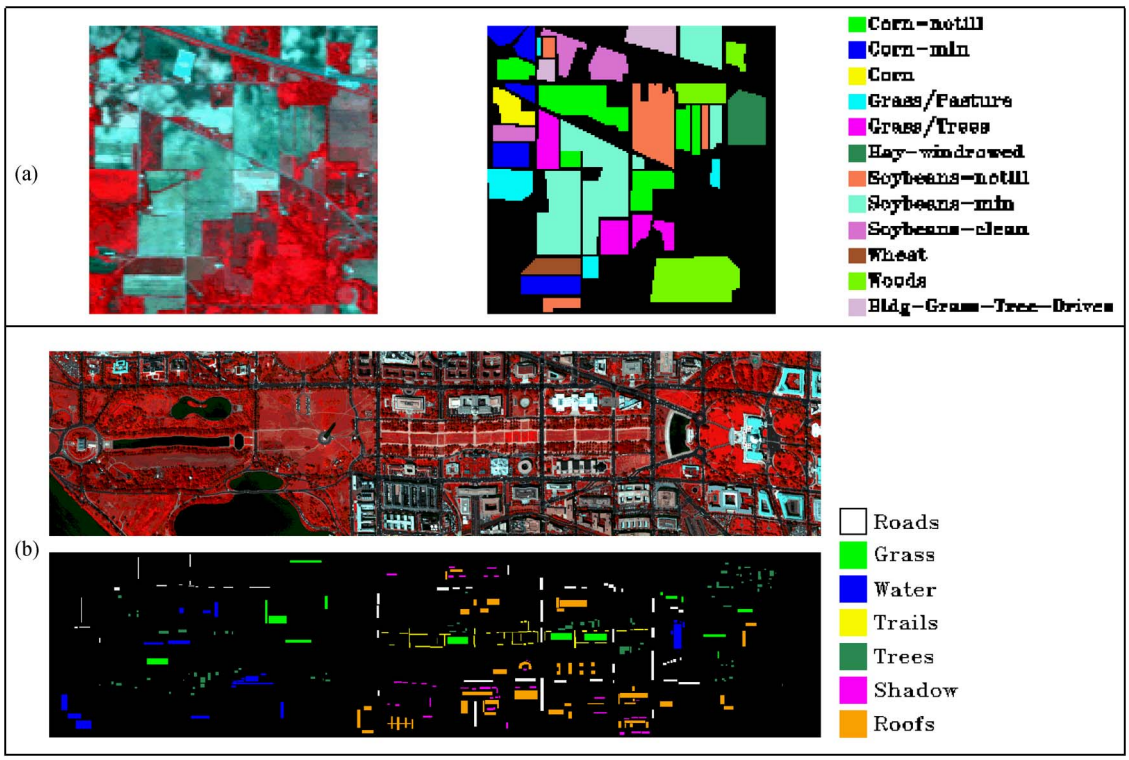

Fig. 4. Hyperspectral data sets of (a) the AVIRIS Indian Pines agricultural area and (b) the HYDICE DC Mall.

TABLE III
NUMBER OF THE VALIDATION SAMPLES (AVIRIS DATA SET)

Class	# Samples
Corn-notill	1,434
Corn-min	834
Corn	234
Grass/Pasture	497
Grass/Trees	747
Hay-windrowed	489
Soybeans-notill	968
Soybeans-min	2,468
Soybeans-clean	614
Wheat	212
Woods	1,294
Bldg-Grass-Tree-Drives	380
Total	10,171

bands with 2.5-m spatial resolution). The water absorption bands were discarded from the original 210 channels in the visible and infrared regions (400–2400 nm), resulting in 191 channels available for the experiments. As shown in Fig. 4(b), this image consists of 1280 × 307 pixels, with 19 332 labeled pixels for model validation (see Table IV). The HYDICE DC Mall image is also a challenging data set for image classification, mainly due to the following reasons: 1) the materials used for constructing rooftops in the scene exhibit large diversity, and hence, no single spectral response can be expected from this class; 2) several groups of classes have similar spectral properties, such as water-shadow, trees-grass, and roofs-trails-roads, which reduces spectral separability and increases classification difficulty.

TABLE IV
NUMBER OF THE VALIDATION SAMPLES (HYDICE DC MALL DATA SET)

Class	# Samples
Roads	3,334
Grass	3,075
Water	2,882
Trails	1,034
Trees	2,047
Shadow	1,093
Roofs	5,867
Total	19,332

2) HSR Data Sets: High spatial resolution (HSR) data provide detailed ground information, and hence, exploitation of the joint spectral–spatial features is imperative for accurate classification in this case. Thus, experiments on the HSR data sets, in particular, are relevant for the evaluation of the considered CPP models, which are constructed on the basis of the neighboring information. In this paper, three HSR data sets are used for validation and comparison of the various algorithms addressed in this contribution. The test images are shown in Fig. 5(a)–(c), respectively, for the QuickBird Wuhan, WorldView-2 Hainan, and ZY-3 Wuhan areas. Their available reference samples are reported in Table V. The challenge for interpreting these HSR images is to discriminate between the spectrally similar classes, e.g., grass-trees, water-shadow, and roads-buildings-soil.

3) SAR: In order to further validate the discussed CPP methods, two SAR data sets are employed in this study. It is interesting to see the performance of the CPP methods for the SAR images, where a large amount of speckle noise exists. The first test image, airborne synthetic aperture radar (AirSAR)

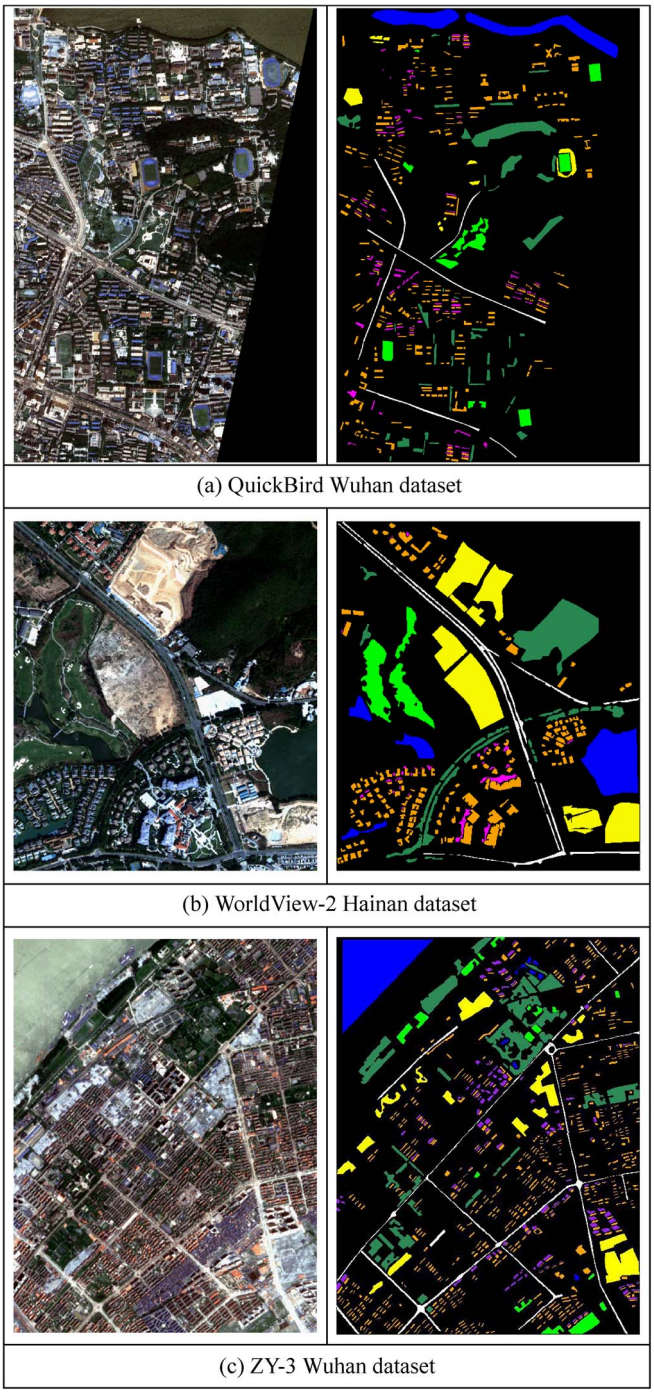

(a) QuickBird Wuhan dataset

(b) WorldView-2 Hainan dataset

(c) ZY-3 Wuhan dataset

Fig. 5. HSR data sets and their reference samples. (a) QuickBird Wuhan. (b) WorldView-2 Hainan. (c) ZY-3 Wuhan.

L-band PolSAR data, was obtained by NASA JPL over the Flevoland site in the Netherlands. The Pauli-RGB image and ground truth are shown in Fig. 6(a). The Flevoland image is a widely used SAR test image for land-cover classification, containing different crop classes as well as bare soil, water, and forest. PolSAR is an advanced form of SAR that emits and receives multifrequency and fully polarized radar waves and has shown advantages in land-cover classification [37]. The other PolSAR image considered in this study was acquired by the Electromagnetics Institute Synthetic Aperture Radar (EMISAR) system over Foulum, Denmark. As shown in the image and its reference data [see Fig. 6(b)], the study area covers a vegetated region, which consists of water, coniferous, rye, oat, and winter wheat. Information for the reference samples of the two SAR test images is provided in Table VI. The challenges for classifying the two SAR images considered in this experiment are twofold: 1) discriminating between the different vegetation species and/or agricultural crops; and 2) smoothing the classification result that is blurred by the speckle noise.

TABLE V
NUMBER OF THE VALIDATION SAMPLES FOR HSR DATA SETS

	# Samples		
Class	QuickBird	WorldView-2	ZY-3
Roads	5,103	5,357	5,932
Grass	9,179	7,417	3,321
Buildings	18,296	11,578	10,065
Soil	3,709	22,189	8,904
Shadow	4,378	1,427	3,629
Trees	17,415	14,086	15,169
Water body	16,614	11,209	11,898
Total	74,694	73,263	58,918

B. Experimental Setup

Our experimental setup first reports the parameters considered for the CPP algorithms and the classification (training samples and classifier). In the following, we report such parameters for the different techniques considered in this work.

1) Filtering:
   - Majority: Window size $w = \{3, 5, 7, 9, 11\}$;
   - Gaussian: Window size $w = \{3, 5, 7, 9, 11\}$, and distance kernel parameter $\sigma = (w - 1)/2$;
   - Bilateral: Window size $w = \{3, 5, 7, 9, 11\}$, distance kernel parameter $\sigma = (w - 1)/2$, and probability kernel parameter $\gamma = \{0.1, 0.2, 0.5, 1, 2, 5, 10, 20\}$;
   - Edge-aware: Window size $w = \{3, 5, 7, 9, 11\}$, distance kernel parameter $\sigma = (w - 1)/2$, and spectral kernel parameter $\gamma = \{0.02, 0.05, 0.1, 0.2, 0.5, 1, 2, 5\}$;
   - Anisotropic diffusion: Iteration number $t = 150$, $\lambda = 0.1$, and parameter $K = \{0.5, 1, 2, 5\}$. Equation (7) is used as the flux function.
2) OBV:
   - OBV-Soft and OBV-Crisp: The spatial bandwidth is adaptively selected according to the pixel shape index [5]. Spectral bandwidth $= \{10, 15, 20\}$, and minimum region size $= \{1, 5, 10, 15, 20, 25, 30\}$.
3) MRF:
   - MRF: Weight of the spatial item $\beta = \{0.05, 0.1, 0.2, 0.5, 1, 2, 5, 10, 20\}$.
4) Relearning:
   - Relearning-PCM and relearning-Hist: Window size $w = \{7, 9, 11\}$.
5) Classification:
   - Classifier: Support vector machine (SVM) is chosen as the base classifier of the CPP algorithms in this

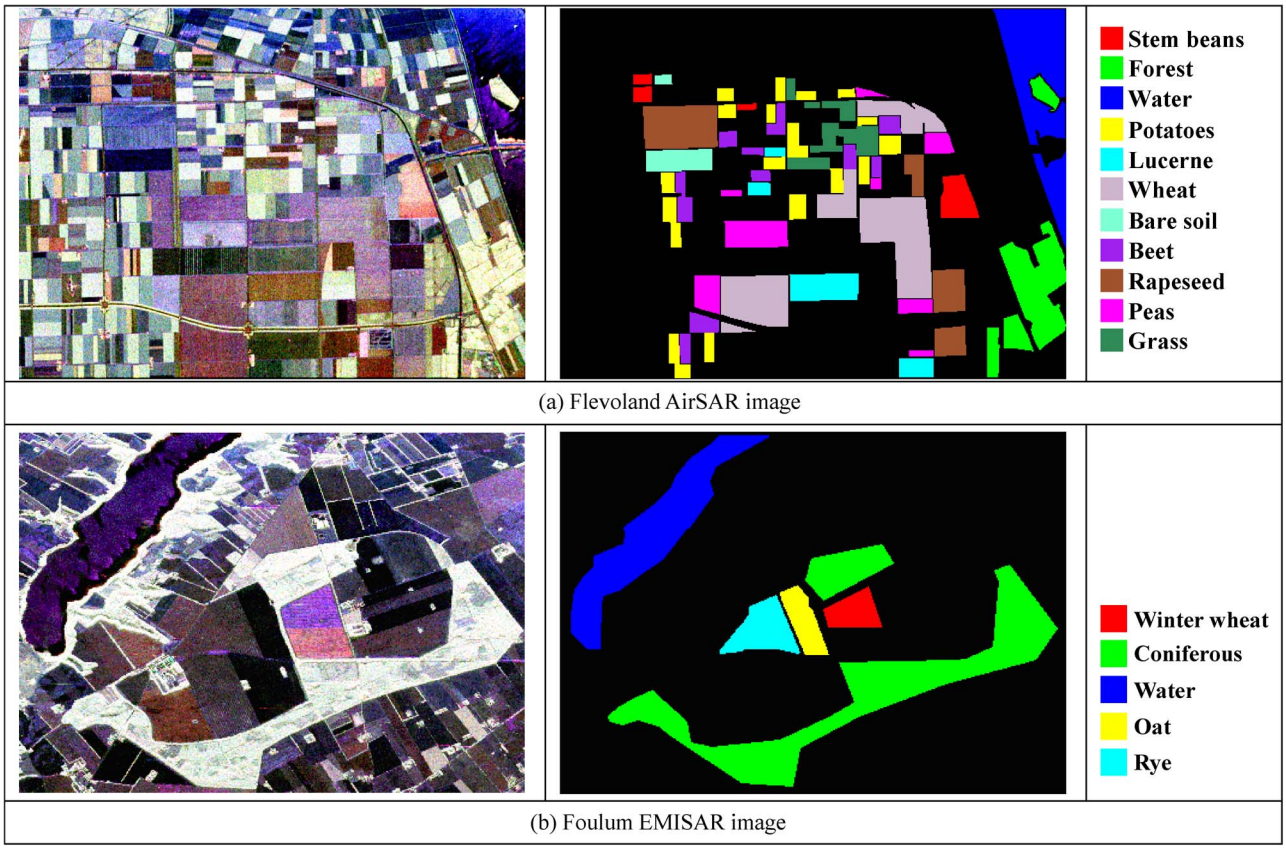

Fig. 6. SAR test images and ground truth references. (a) Flevoland AirSAR. (b) Foulum EMISAR.

TABLE VI
NUMBER OF VALIDATION SAMPLES (SAR DATA SETS) FOR (a) FLEVOLAND AIRSAR AND (b) FOULUM EMISAR

(a)

Class	# Samples
Stem beans	1,932
Forest	6,423
Water	7,925
Potatoes	5,379
Lucerne	3,004
Wheat	11,482
Bare soil	1,604
Beet	3,409
Rapeseed	6,129
Peas	4,264
Grass	2,725
Total	54,276

(b)

Class	# Samples
Winter wheat	1,088
Coniferous	12,851
Water	6,695
Oat	1,172
Rye	1,767
Total	23,573

study because it is a rapid and adaptive learning approach that does not require prior assumptions on the distribution of input features [8], [11]. The parameters of the SVM are: Penalty coefficient $= 100$, kernel $=$ RBF (radial basis function), RBF bandwidth $\sigma = 1/n$ (n is the dimension of the input features).

- Training and test samples: 50 and 100 samples per class selected from the reference are used for training of the SVM for the hyperspectral and HSR data sets, respectively. As for the SAR experiments, 20 samples per class are adopted. The rest of the samples are used for the validation of the various algorithms.

The parameter sensitivity is analyzed in Section V-B.

V. EXPERIMENTS

This section presents the general experimental results of the CPP methods, with their parameter sensitivity analysis and a visual comparison, followed by a detailed comparison between the CPP methods and the current mainstream spectral–spatial classifications. In particular, the proposed relearning methods are analyzed in detail.

A. General Results

The general results obtained by the CPP algorithms investigated in this study are provided in Table VII. Two commonly used measures, namely, the overall accuracy (OA) and the Kappa coefficient, were extracted from the confusion matrix for quantitative assessment. Due to the high correlation between

TABLE VII
OVERALL ACCURACY (%) OF THE CPP ALGORITHMS INVESTIGATED IN THIS STUDY FOR THE VARIOUS REMOTE SENSING DATA SETS. THE MEAN AND STANDARD DEVIATION OF THE OA VALUES FOR EACH CPP ALGORITHM ARE REPORTED BASED ON 30 RUNS WITH DIFFERENT STARTING TRAINING SETS. THE STANDARD DEVIATIONS ARE REPORTED IN THE BRACKETS

CPP	Algorithm	Hyperspectral images		High spatial resolution images			SAR images	
		AVIRIS	HYDICE	QuickBird	WV-2	ZY-3	AirSAR	EMISAR
Raw	Raw	61.7 (2.2)	89.6 (1.4)	85.6 (0.7)	90.7 (0.8)	86.4 (0.5)	80.4 (1.7)	93.4 (0.9)
Filtering	Majority	75.7 (3.3)	91.6 (1.4)	86.3 (0.9)	92.5 (1.0)	89.8 (0.7)	85.4 (1.8)	97.1 (0.6)
	Gaussian	74.4 (2.3)	95.1 (0.9)	85.7 (0.8)	94.3 (1.1)	88.3 (0.7)	84.0 (1.5)	98.1 (0.8)
	Bilateral	76.0 (2.5)	95.6 (0.9)	85.8 (0.8)	94.6 (1.2)	90.5 (0.5)	84.2 (1.5)	98.1 (0.8)
	Edge	75.5 (2.3)	95.3 (1.0)	86.2 (0.9)	94.6 (1.2)	90.2 (0.5)	84.1 (1.5)	98.1 (0.8)
	Anisotropic	77.7 (2.4)	95.4 (0.9)	85.8 (0.8)	94.7 (1.2)	89.9 (0.5)	85.4 (1.5)	99.2 (0.6)
OBV	OBV-Crisp	73.3 (3.4)	92.1 (1.7)	86.1 (1.1)	91.7 (1.0)	88.6 (0.6)	89.2 (2.3)	96.7 (0.3)
	OBV-Soft	71.6 (2.9)	94.2 (1.3)	86.2 (1.1)	92.8 (0.9)	88.1 (0.7)	88.3 (2.4)	96.4 (0.2)
Random field	MRF	78.2 (2.4)	96.8 (1.5)	85.6 (0.7)	95.3 (1.8)	89.5 (0.7)	85.2 (1.8)	98.5 (0.4)
Relearning	Relearning-Hist	91.5 (2.0)	98.2 (0.9)	96.8 (0.4)	98.3 (0.5)	96.0 (0.4)	87.2 (1.3)	99.3 (0.7)
	Relearning-PCM	93.1 (1.1)	98.5 (1.0)	95.9 (0.7)	98.4 (0.3)	95.4 (0.4)	87.5 (1.3)	99.2 (0.6)

TABLE VIII
STATISTICAL SIGNIFICANCE TEST FOR THE SEVEN EXPERIMENTS IN THIS STUDY
(' + ' = positive significance, 'N' = No significance, ' − ' = negative significance)

	Filter					OBV		RF	Relearning	
	Majority	Gaussian	Bilateral	Edge	Aniso-	Crisp	Soft	MRF	Hist	PCM
Raw	3N,4–	2N,5–	2N,5–	2N,5–	1N,6–	3N,4–	2N,5–	2N,5–	7–	7–
Majority		6N,1–	6N,1–	6N,1–	5N,2–	7N	7N	6N,1–	1N,6–	1N,6–
Gaussian			6N,1–	6N,1–	7N	7N	7N	7N	2N,5–	2N,5–
Bilateral				7N	7N	1+,6N	1+,6N	7N	2N,5–	2N,5–
Edge					7N	1+,6N	1+,6N	7N	2N,5–	2N,5–
Aniso-						1+,6N	2+,5N	7N	2N,5–	2N,5–
OBV-Crisp							7N	5N,2–	1N,6–	1N,6–
OBV-Soft								6N,1–	1N,6–	1N,6–
MRF									4N,3–	4N,3–
Hist										7N

OA and Kappa, only the OA values are reported in the table. Note that the accuracy of each algorithm is presented with its optimal parameters. All the experiments are repeated 30 times with different starting training sets. This way, the mean and standard deviation of the OA for each CPP algorithm are reported in Table VII. Moreover, tests for statistical significance have been performed, and the results of the z-scores [38] are reported in Table VIII, where the symbol "+", "N", and "−" denote positive $(z > 1.96)$, no $(-1.96 \leq z \leq 1.96)$, and negative $(z < -1.96)$ statistical significance, respectively. For instance, "6N, 1-" for the "majority vs. Gaussian" signifies that the majority filter obtains 6 no significance and 1 negative significance in the seven experiments when compared with the Gaussian filter.

The first noteworthy observation from the results reported in Table VII is that the proposed relearning methods achieve the highest accuracy values except for the AirSAR data set when compared with the other CPP methods. Furthermore, it should be noted that the accuracy improvements are strikingly significant. For instance, compared with the raw classification, the average improvements obtained by the relearning-PCM are 31.4% (AVIRIS), 8.9% (HYDICE), 10.3% (QB), 7.7% (WV-2), 9.0% (ZY-3), 7.1% (AirSAR), and 5.8% (EMISAR). This conclusion is also supported by the significance test shown in Table VIII, since all the other CPP methods obtain "N" and "−" significance compared with relearning. The satisfactory performance of the relearning methods is due to their ability to enhance class separability. The traditional CPP algorithms, such as MRF, filtering, and voting, however, are only able to smooth the classification results and reduce the salt-and-pepper effect.

From Tables VII and VIII, first of all, it can be seen that all the CPP methods can provide higher accuracy values to varying degrees, compared with the raw classification. The proposed relearning methods obtain significantly better results than raw classification in all the experiments, and this is followed by anisotropic diffusion, giving 6 positive significance scores in seven tests.

Among the five filtering methods, the "N" value is dominant, showing that they provide similar accuracy values in most cases. Nevertheless, it should be stated that the anisotropic, edge-aware, and bilateral filters achieve slightly better results than the majority method, since the former show slightly higher accuracy values (up to 4%) and $1 \sim 2$ positive significance scores in seven experiments.

The OBV methods achieve significantly better results than the raw classification ($4 \sim 5$ positive significance scores), similar accuracy values with the majority and Gaussian filters

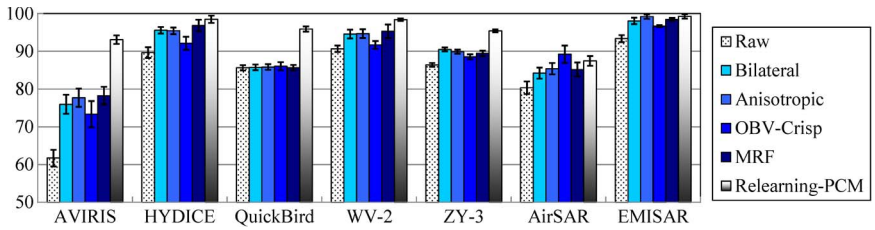

Fig. 7. Comparison between the representative CPP algorithms in all the experiments, with the horizontal and vertical axes being the test images and the obtained OA values, respectively.

(7 "N" values), but slightly worse results than the bilateral, edge-aware, anisotropic filters and the MRF method ($1 \sim 2$ negative scores), in terms of the tests in Table VIII. In particular, from Table VII, it is noticed that the OBV algorithms outperform the other CPP methods in the Flevoland AirSAR image, which can be attributed to its high-quality segmentation owing to the regular croplands with uniform shape. This phenomenon shows that the performance of the OBV strongly relies on the quality of the segmentation. In addition, from Tables VII and VIII, it can be seen that the OBV-Soft does not show obvious advantages over the OBV-Crisp in all the experiments, which shows that the different strategies used for the voting (based on class probability or label) do not have a significant impact on the OBV.

As for the MRF, it can be seen that it performs equally well with the filtering methods, but slightly better than the OBV since $1 \sim 2$ positive significance values are obtained. Compared with the raw classification, the increments of the OA achieved by the MRF are 16.5% (AVIRIS), 7.2% (HYDICE), 0.0% (QuickBird), 4.6% (WV-2), 3.1% (ZY-3), 4.8% (AirSAR), and 5.1% (EMISAR), respectively.

Concerning the relearning strategy, the two proposed algorithms yield very promising results in terms of their OA values, which are higher than 90% in nearly all the experiments. Specifically, among all the 63 significance tests (seven experiments compared with the other nine methods), 70% are positive significance, and the remaining 30% are no significance, without negative scores reported. The two relearning algorithms achieve similar results in terms of the accuracy values in Table VII and the statistical test in Table VIII.

The OA values with the standard deviations for several representative CPP algorithms are compared in Fig. 7, where the horizontal and vertical axes indicate the test images and the obtained OA values, respectively. From the figure, the superiority of the relearning strategy compared to other CPP algorithms can be clearly seen. Moreover, it results in high accuracies but low standard deviations, which reveals that the relearning-PCM is effective and robust. In addition, it can also be seen that the anisotropic diffusion obtains comparable results to the MRF, and, the bilateral filter also produces satisfactory results.

In Fig. 7, it can be seen that the QuickBird data set represents a special case, mainly because all the CPP algorithms do not show any improvement with regard to the raw classification, except for the relearning strategies. To further explore this issue, the confusion matrices for the QuickBird data set obtained by the raw classification, MRF, and relearning-PCM are presented in Table IX. Such confusion matrices show that the classification errors mainly point to the discrimination between buildings, roads, and soil, which are spectrally similar. From the tables, it can be also seen that when the relearning-PCM algorithm is used, the misclassifications between the spectrally similar classes are significantly reduced. For instance, the errors for roads-buildings are 3350, 3331, and 504 pixels, respectively, for the raw, MRF, and relearning-PCM. Furthermore, the situation is similar for the cases of buildings-roads, trees-grass,

TABLE IX
CONFUSION MATRICES FOR THE QUICKBIRD DATA SET: (a) RAW CLASSIFICATION, (b) MRF, AND (c) RELEARNING-PCM. THE CONFUSION MATRIX WITH THE HIGHEST ACCURACY IN 30 RUNS IS REPORTED FOR EACH METHOD

(a) Raw classification, OA = 87.2%, $k = 0.845$

	Building	Roads	Trees	Grass	Water	Soil	Shadow
Building	12041	1458	5	1	0	326	5
Roads	3350	3585	1	0	22	152	26
Trees	1	0	16685	323	0	0	6
Grass	11	7	599	8780	0	29	0
Water	1	6	0	0	16561	0	22
Soil	2867	33	4	75	0	3202	4
Shadow	25	14	121	0	31	0	4315

(b) MRF, OA = 87.3%, $k = 0.846$

	Building	Roads	Trees	Grass	Water	Soil	Shadow
Building	12066	1459	4	1	0	325	5
Roads	3331	3587	1	0	21	152	25
Trees	1	0	16698	317	0	0	6
Grass	11	7	593	8789	0	28	0
Water	1	6	0	0	16564	0	22
Soil	2861	31	4	72	0	3204	4
Shadow	25	13	115	0	29	0	4316

(c) Relearning-PCM, OA = 97.4%, $k = 0.969$

	Building	Roads	Trees	Grass	Water	Soil	Shadow
Building	17287	154	79	0	0	26	28
Roads	504	4949	2	6	27	47	0
Trees	11	0	16910	22	0	5	12
Grass	10	0	422	9128	0	47	0
Water	0	0	0	0	16587	0	0
Soil	250	0	2	23	0	3584	0
Shadow	234	0	0	0	0	0	4338

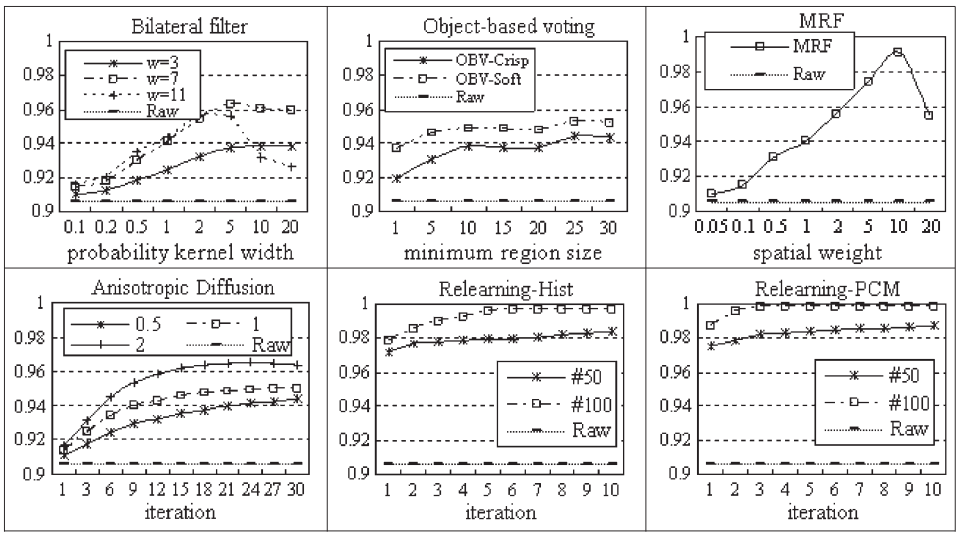

Fig. 8. Analysis of the parameter sensitivity for the CPP methods considered in this study. The training samples (50 pixels for each class) used to generate the accuracy curves are randomly chosen from the reference. For the bilateral filter, the accuracy curves represent different window sizes ($w = 3, 7, 11$). For the anisotropic diffusion, the accuracy curves represent the parameter $K = 0.5, 1, 2$, defined in (7). In the relearning methods, the curves stand for the accuracy values achieved by different sizes of training samples (50 and 100 samples for each class, i.e., #50, and #100).

buildings-soil, and roads-soil, where the misclassifications obviously decrease with the relearning-PCM method. The QuickBird experiment in Table IX is a good example to show the superiority of the proposed relearning strategy for enhancing the separability between similar classes and improving the raw classification.

B. Parameter Sensitivity Analysis

This section discusses how the parameters of the CPP algorithms influence their performance. Fig. 8 shows the OA of some representative CPP methods over a range of parameters with the HYDICE DC Mall data set. The HYDICE image is chosen for the analysis of parameter sensitivity because it is a hyperspectral image with high spatial resolution, and hence, it is representative of the data sets used in this study. In Fig. 8, we can once again clearly observe the general performance of the CPP algorithms: 1) all the postprocessing algorithms show obviously higher accuracy values than the raw classification; 2) the relearning methods achieve steady and accurate classification results; and 3) the random field, bilateral filter, and the anisotropic diffusion can provide satisfactory accuracy values when their parameters are well tuned. Detailed discussions are given below.

1) Bilateral filter: A larger window size and kernel width lead to higher accuracy values, showing that successful application of the bilateral filter is based on a sufficient characterization of contextual information around each pixel. However, the parameters for the neighboring response should be carefully tuned. For instance, in this experiment, the window size of 7 with a probability kernel width of 5 yields the optimal result ($\mathrm{OA} = 96.3\%$).
2) OBV: The minimum region size does not influence the final result as the values in a range of 10–30 lead to similar accuracy values.
3) MRF: It can be seen that the spatial weight, which defines the degree for penalizing the dissimilarity in a neighborhood, has an obvious impact on the classification accuracy. It should be carefully chosen for an effective MRF implementation.
4) Anisotropic diffusion: In Fig. 8, the curves represent the accuracy values achieved by different values of the coefficient K, defined in (7). As previously stated, the value of K can be viewed as an indicator that defines the degree of anisotropy in the diffusion, e.g., a larger value signifies a more isotropic diffusion. Consequently, the value of K should be selected according to the spatial characteristics of the image scenes. For instance, in the case of the HYDICE data set considered in this experiment, the largest value ($K = 2$) has the optimal accuracy curve, since the DC Mall image exhibits a relatively isotropic landscape [see Fig. 4(b)], where buildings with rectangular shape are regularly arranged. In addition, it can be seen that the anisotropic diffusion needs about 30 iterations to reach convergence.
5) Relearning: The accuracy values obtained by the two newly developed relearning algorithms are consistently high in all cases. Note that the relearning methods with only one iteration can significantly increase the OA of the raw classification, i.e., from 90% to 98%. By comparing the relearning-PCM and the relearning-Hist, it can be seen that the former performs better and converges faster than the latter. Only three iterations are needed for PCM to achieve a stable status. It is therefore implied that the consideration of the spatial arrangement of primitives can enhance the performance and accelerate convergence of the relearning algorithm. In addition, the performance of the relearning methods with different training sets has been also tested. As the accuracy curves in Fig. 8 show, the increase in the number of training samples from 50 to 100 (per class) leads to an increment of the OA by $1 \sim 2\%$ (on average). After three iterations, the relearning-PCM with 100 training samples per class can achieve almost perfect classification accuracy (over 99.5%).

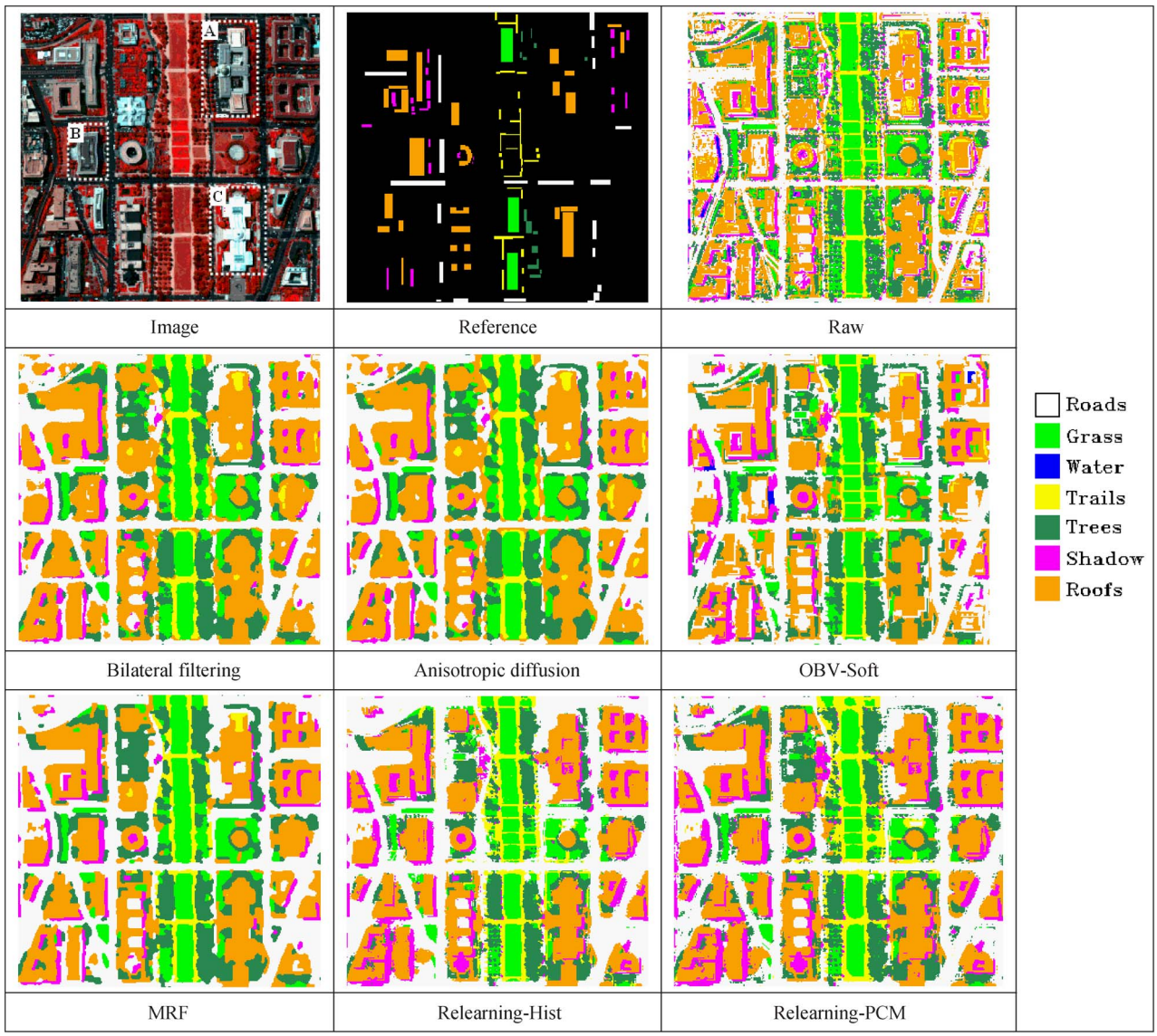

Fig. 9. Subset images of the classification maps for the HYDICE DC Mall image.

C. Visual Comparison

In addition to the accuracy values given in the previous section, this section provides a visual comparison of the results obtained by the CPP algorithms considered in this study. For the HYDICE DC Mall image, the classification maps of the subimages extracted are compared in Fig. 9. A detailed discussion of the performance of each CPP algorithm follows.

1) Raw classification: The salt-and-pepper effect can be clearly seen for the pixelwise classification. Meanwhile, a lot of misclassifications occur between water-shadow and trails-roofs due to their similar spectral reflectance.
2) Bilateral filtering: Compared with the raw result, the misclassifications in regions A, B, and C are partly corrected by the bilateral filter, and the confusion between water and shadow is also clarified. The improvements can be attributed to the fact that the probability information in the neighborhoods is effectively exploited in postprocessing. However, it can be also observed that misclassifications still exist, e.g., roof A is partially identified as trails.
3) Anisotropic diffusion: This produces a similar classification map to the bilateral filter.
4) OBV-Soft: Although this approach is effective in suppressing the salt-and-pepper noise of the pixelwise classification, it fails to discriminate between roads, roofs, and trails.
5) MRF: It achieves satisfactory result, and the classification map looks clear. The classification errors between roofs-trails-roads are substantially reduced (see roofs A, B, and C). However, some errors are not corrected, e.g., the confusion between roofs and trails in roof A. As revealed in [18], the CPP methods based on the smoothness assumption tend to oversmooth small structures to some extent. In this regard, it can be observed that the classification maps generated by the filters and MRF do not exhibit clear boundaries between adjacent objects.
6) Relearning: The relearning-Hist and relearning-PCM algorithms give very similar classification maps, where the errors in regions A, B, and C have been totally rectified. Moreover, the misclassifications between water and

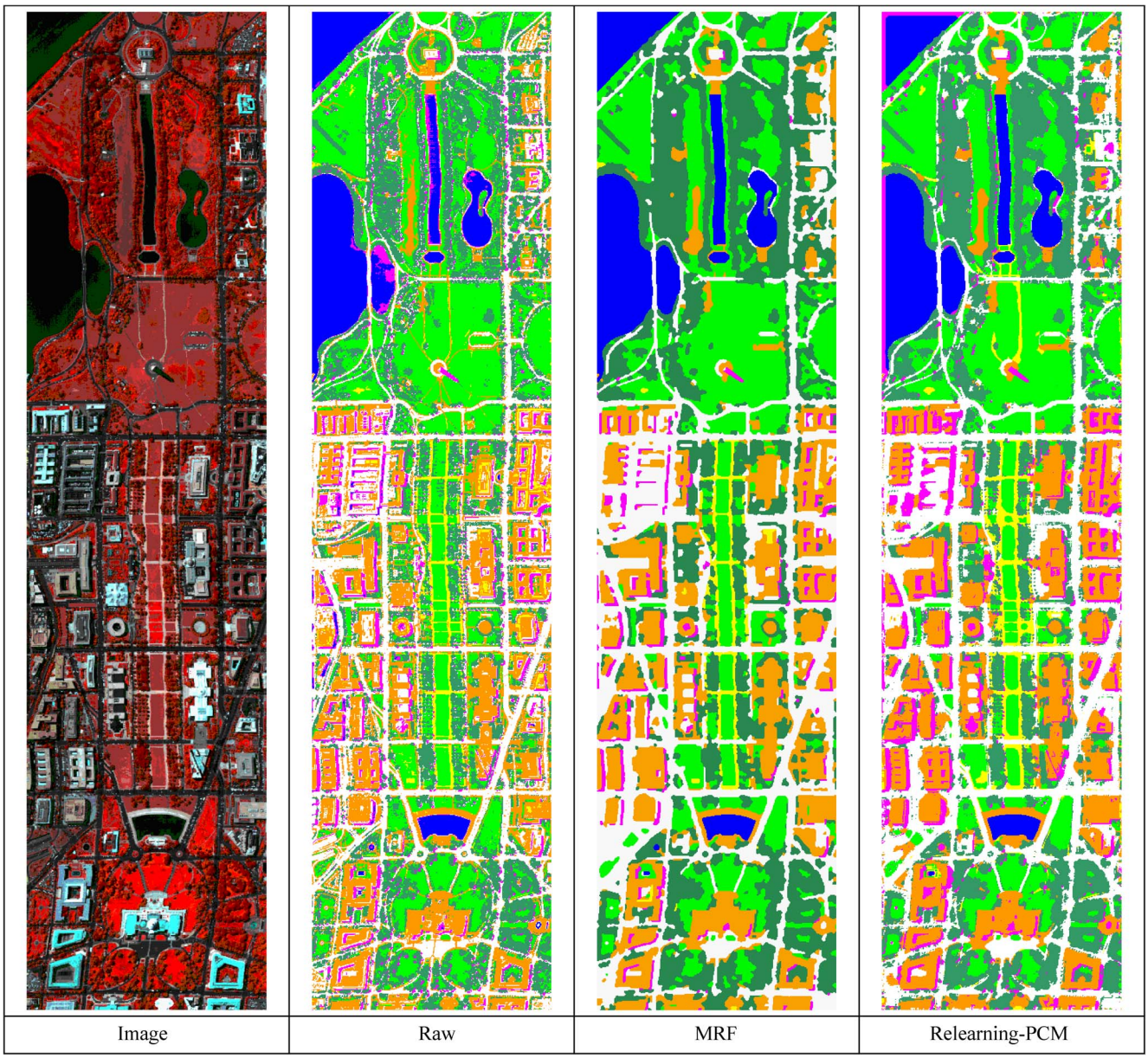

Fig. 10. Classification maps of the HYDICE DC Mall data set obtained by raw classification, MRF, and relearning-PCM methods.

shadow have been corrected. Compared with the results achieved by the filters and MRF, the boundaries between adjacent objects are clearer, and the shape of structures is delineated better with the relearning methods.

Moreover, the classification maps of the whole image by raw, MRF, and relearning-PCM methods are displayed in Fig. 10. The MRF and relearning algorithms are of particular interest since they achieve the most accurate results in the DC Mall test and even in all the experiments. It can be observed that relearning is more effective for improving the raw classification than MRF and, at the same time, better at preserving the detailed structures and edges. The satisfactory performance of the relearning-PCM can be attributed to the fact that this method is able to learn the implicit rules of spatial arrangement of primitives.

The WorldView-2 Hainan data set is also taken as an example for the visual comparison of the results of the CPP algorithms (Fig. 11). In this case, two regions (A and B) are the focus of our study. Region A is related to the confusion between buildings and roads. It can be seen that the filtering and OBV methods rely on the initial classification result, where some buildings in region A were wrongly classified as roads. The MRF method correctly identifies the buildings, but it causes oversmoothing effects in this region, e.g., the shadows are merged with the buildings nearby. This way, the whole region is classified as buildings and detailed structures (e.g., shadow and shape of roofs) are lost. On the other hand, in Fig. 11, it can be seen that the proposed relearning methods are able to solve the misclassification problems, since most of the buildings in region A are now correctly identified. The case of region B is similar to region A, in which a number of building pixels are wrongly classified as soil by the raw, filtering, and OBV algorithms, but are correctly identified by the relearning methods. Therefore, the WorldView-2 experiment also shows that only the

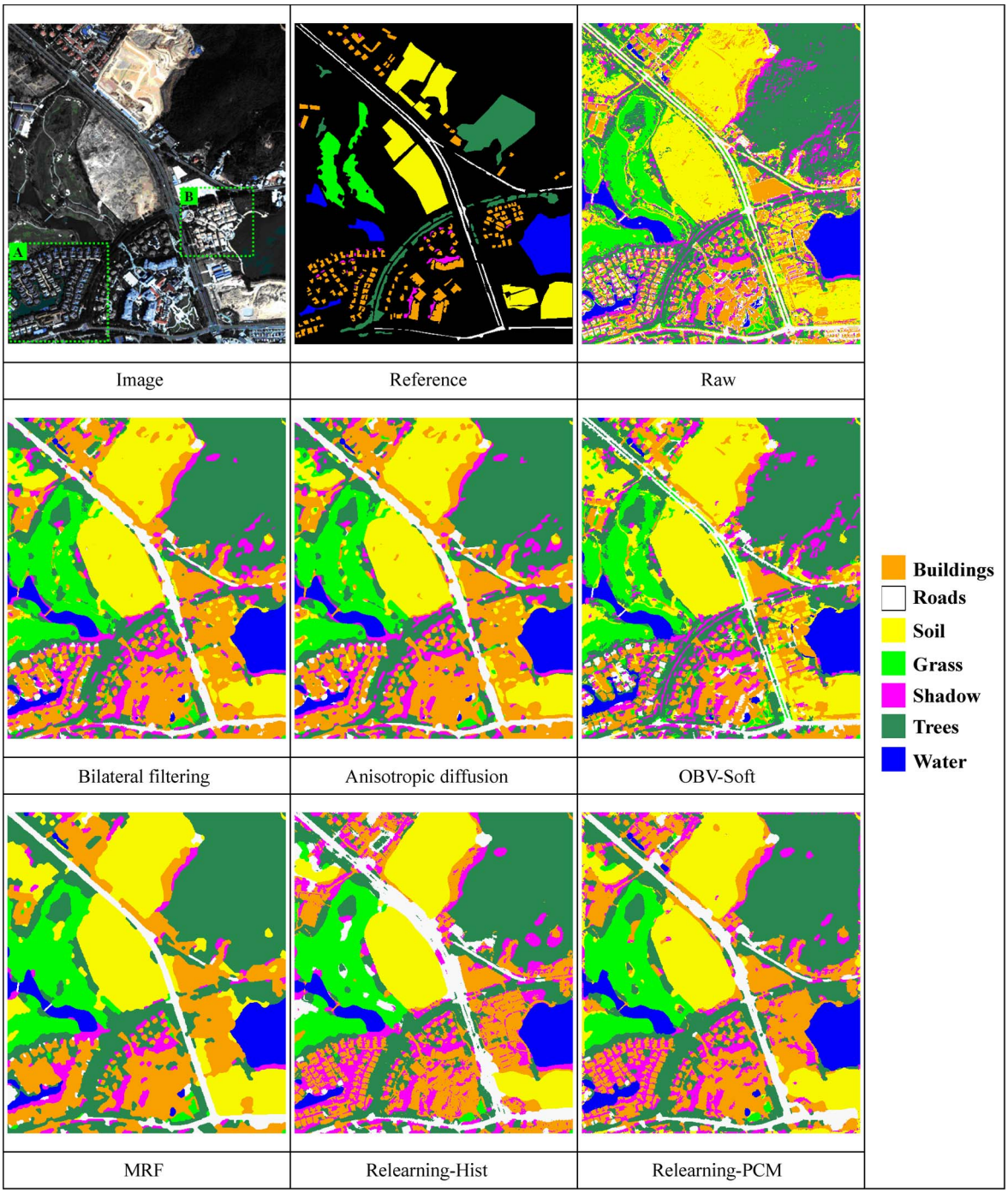

Fig. 11. Classification maps for the CPP algorithms with the WordView-2 Hainan data set.

relearning methods (among all the CPP strategies considered in this study) can provide sufficient discriminative ability for the classification and avoid the oversmoothing effects.

The classification results for the Foulum EMISAR data set are shown in Fig. 12. Only the reference regions are displayed, according to the distributor of the data set [39]. It should be kept in mind that the main task of postprocessing in this experiment is to smooth the initial result, since the raw classification is already quite good (average OA $= 93.4\%$). From this point of view, it can be seen that the anisotropic diffusion, MRF, and the relearning methods achieve very accurate classification maps, except that a few boundaries on the water body are incorrectly identified by the MRF. The visual inspection is in agreement with the quantitative accuracy values presented in Table VII.

D. Analysis of Relearning Methods

Here, a classification certainty analysis is conducted, in order to analyze the mechanism of the proposed relearning methods. The certainty Cert(x) for each pixel x can be described by the margin of the classifier, i.e., the difference between the two highest probabilities

$$\text{Cert}(x) = \max_{i \in C}(p_{x,i}) - \max_{i \in C \setminus w^+}(p_{x,i}) \tag{13}$$

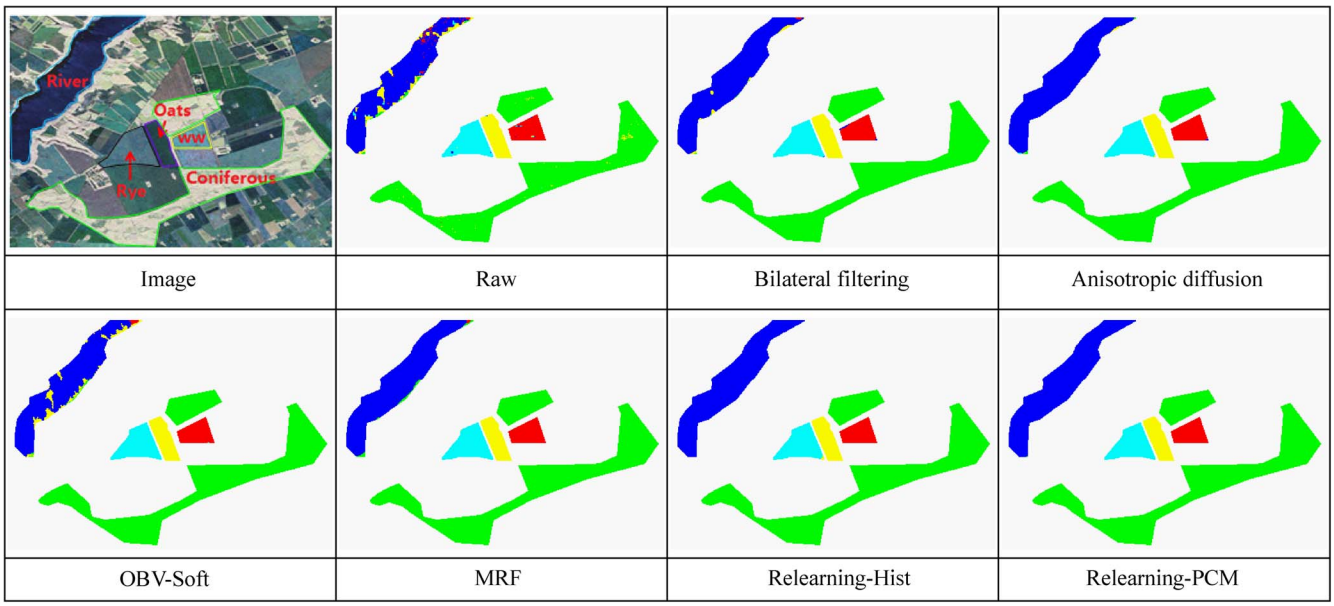

Fig. 12. Classification results for the CPP algorithms with the Foulum EMISAR data set (blue = water, cyan = rye, yellow = oat, green = coniferous, red = winter wheat). The original image and the ground truth are provided by the authors in [39].

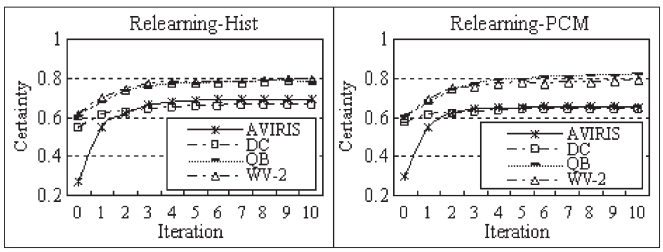

Fig. 13. Classification certainty values of the relearning methods for different test images.

where w^+ denotes the class having maximal probability, i.e., the first item of (13). A larger value of $\mathrm{Cert}(x)$ shows more reliable decision on the pixel x. The average classification certainty values are reported in Fig. 13 for the two relearning methods, where "Iteration = 0" denotes the raw classification without relearning. It can be clearly seen that both relearning algorithms can significantly raise the certainties of the raw classification, and it tends toward stability after $3 \sim 4$ iterations. By comparing Figs. 8 and 13, it can be found that the increase in the margin (or certainty) corresponds to the increase in the classification accuracy.

Moreover, in Fig. 14, a graphic example is provided in order to show how the relearning methods improve the raw classification iteratively. The focus of the example is on the shadows in the leftmost part of the image, which were incorrectly classified as water by the raw method, and on the roof in the middle, which were incorrectly identified as roads by the raw classification. Analyzing the classification certainty (the first row), it can be observed that the values in the considered regions (i.e., the shadows and roofs) become larger (brighter), corresponding to the decrease in the errors observed from the classification maps (the second row). Specifically, the misclassifications between roads and roofs are gradually improved from iteration = 0 to 4, and the results remain stable from iteration 4 to 10.

Another example is shown in Fig. 15. The classification errors in this case occur between water and shadows and roofs and trails. It can be similarly seen that the classification certainty is gradually raised by the relearning algorithm. At the same time, the classification maps are significantly improved compared with the raw method (i.e., Iteration = 0), and in this example, the results are steadily accurate from Iteration = 2 to 10.

E. Comparison

The experiments reported in previous subsections show that the proposed CPP relearning algorithms are able to learn the intrinsic rules or patterns in the raw classification result and then provide more discriminative information and improve the classification. Although the basic point of view of the relearning is different from the commonly used spectral–spatial classifications, they are both effective for enhancing class separability by considering the neighboring information. Thus, it is meaningful to conduct a comparative study between the relearning methods and the spectral–spatial classifications.

The hyperspectral data sets (AVIRIS Indian Pines data set and the HYDICE DC Mall data set) are public and well-known validation data sets for remote sensing image classification. Therefore, we can conveniently carry out the comparison based on the existing literature.

In the AVIRIS data set (Table X), four sophisticated spectral–spatial classification algorithms are presented. Note that all the methods were tested on the same reference samples.

1) MSSC-MSF (MSSC = multiple spectral–spatial classifier, MSF = minimum spanning tree): The main principle of this approach is to use an ensemble of classifiers to generate a set of so-called markers, i.e., the most reliably classified objects [40]. Subsequently, the marker-controlled region growing, based on the MSF, is used for identification of the unreliable objects.

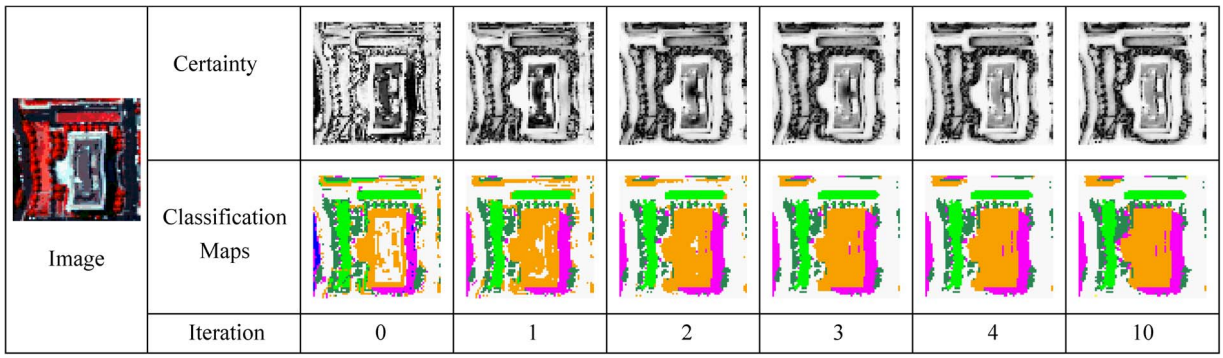

Fig. 14. Classification maps as well as their certainties for the relearning-PCM method (Example 1). Note that the bright and dark components correspond to the high and low classification certainty, respectively (blue = water, magenta = shadow, white = roads, orange = roofs, light green = grass, sea green = trees, yellow = trails).

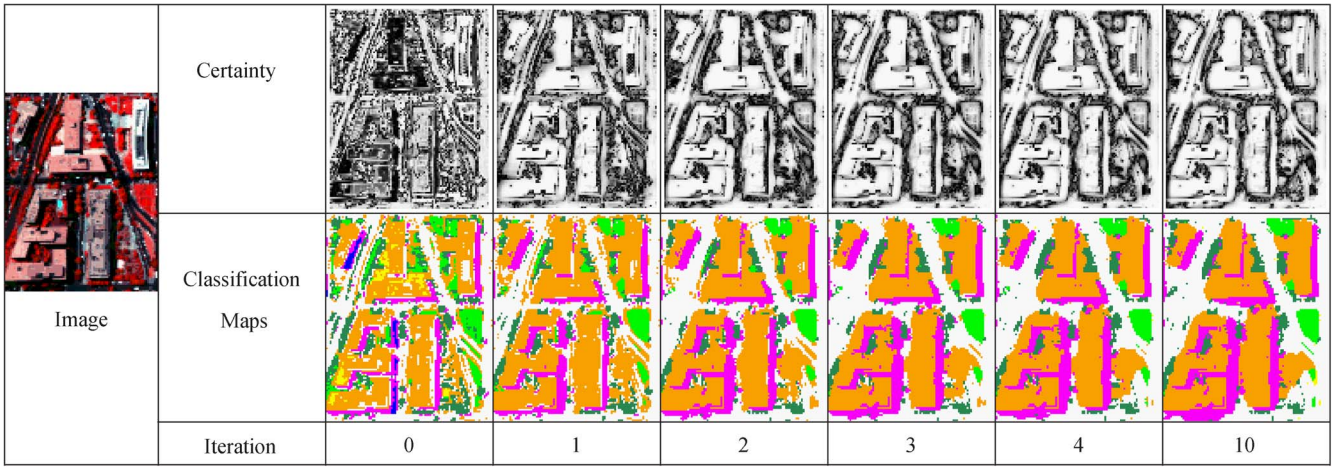

Fig. 15. Classification maps as well as their certainties for the relearning-PCM method (Example 2).

TABLE X
COMPARISON BETWEEN EXISTING TECHNIQUES FOR SPECTRAL–SPATIAL CLASSIFICATION AND THE CPP ALGORITHMS CONSIDERED IN THIS STUDY USING THE AVIRIS INDIAN PINES IMAGE ("# TRAINING" INDICATES THE NUMBER OF TRAINING SAMPLES PER CLASS USED IN THE CORRESPONDING EXPERIMENT)

	MSSC-MSF	ECHO	WLC-GA	Relearning-Hist	Relearning-PCM
# Training	50	50	65	50	50
OA (%)	92.3	82.6	90.7	91.5	93.1

TABLE XI
COMPARISON BETWEEN EXISTING TECHNIQUES FOR SPECTRAL–SPATIAL CLASSIFICATION AND THE CPP ALGORITHMS CONSIDERED IN THIS STUDY USING THE HYDICE DC MALL IMAGE

	VS-SVM	C-voting	P-fusion	OBSA	Relearning-Hist	Relearning-PCM
# Training	100	100	100	100	50	50
OA (%)	94.8	93.9	94.4	98.5	98.2	98.5

2) ECHO (extraction and classification of homogeneous object): This is a well-known spatial classifier that exploits the neighboring information for classification [41].
3) WLC-GA (WLC = weighted linear combination, GA = genetic algorithm): Multiple classification methods are combined by weighting each method according to its contribution to the combination process [42]. Specifically, a weighted linear combination optimized by a genetic algorithm is used to determine the weight or contribution of each classifier.

From Table X, it can be seen that the relearning-PCM outperforms the other methods in terms of the OA values. Meanwhile, the relearning-Hist achieves significantly higher OA than the ECHO classifier and slightly better result than WLC-GA.

In the HYDICE DC Mall data set (Table XI), four advanced spectral–spatial classification algorithms, based on a series of multifeature fusion strategies [8], are employed for comparison with the proposed relearning methods:

1) VS-SVM (VS = vector stacking): The spectral information stacked with the GLCM, differential morphological profiles (DMP) [43], and the 3-D wavelet features [44] is fed into an SVM for the classification. Vector stacking is a simple but efficient approach for integrating multiple spectral–spatial features [45].

TABLE XII
COMPARISON BETWEEN THE EXISTING SPECTRAL–SPATIAL CLASSIFICATIONS AND THE CPP ALGORITHMS FOR THE HSR DATA SETS (QUICKBIRD AND WV-2)

	DMP	OBIA	GLCM	MIL	Relearning-Hist	Relearning-PCM
QuickBird	91.1	92.8	91.9	92.2	96.8	95.9
WV-2	91.3	91.2	83.5	92.9	98.3	98.4

2) C-voting (certainty voting): The SVM-based multiple classification system constructed from the aforementioned GLCM, DMP, and 3-D wavelet features is used to divide the images objects into reliable and unreliable ones. The labels of the unreliable objects are then determined according to the classifier with the highest degree of classification certainty [8].
3) P-Fusion: This is a soft version of C-voting. The certainty degree of each classifier is used as the weight of their probabilistic output. Subsequently, the weighted probabilistic outputs of the classifiers are fused to identify the labels of the unreliable regions [8].
4) OBSA (object-based semantic analysis): The reliable objects are classified via the P-fusion algorithm, whereas the unreliable ones are identified using a set of predefined semantic rules [8].

From Table XI, it can be seen that the relearning-PCM yields the best result, which is significantly better than VS-SVM, C-voting, and P-fusion. The relearning-Hist also gives a high degree of accuracy, which is similar to OBSA and higher than the other methods. Note that although OBSA can produce a satisfactory result, it is dependent on the quality of the segmentation and the definition of the specific rule set. The relearning methods, however, can learn the underlying rules according to the frequency and spatial arrangement of the classified image, instead of empirically setting a set of rules. In addition, by comparing the results in Tables VII and XI in this experiment, it can be seen that most of the CPP methods (e.g., Gaussian, bilateral, edge-aware filters, and MRF) achieve higher accuracy values ($> 95\%$) than the spectral–spatial classifiers such as VS-SVM, C-voting, and P-fusion.

In order to further verify the effectiveness of the considered CPP methods, a comparative study is also carried out for three HSR data sets (Table XII). The spectral–spatial classification methods used for this experiment are briefly introduced.

1) DMP/GLCM: The DMP and GLCM features combined with the spectral information are fed into an SVM for classification.
2) OBIA: An adaptive mean-shift procedure [12] is used to segment the image, and a series of spectral and spatial properties (including the mean, standard deviation, length, width, compactness, solidity, length-width ratio, and extent) are generated for each segment and then concatenated for the subsequent SVM classification.
3) MIL (multi-index learning) [46]: The principle of this approach is to describe an image scene using a set of low-dimensional semantic indexes that replace the traditional high-dimensional and low-level features. The primitive indexes include the morphological building/shadow index [47], the normalized difference vegetation index, and the spectral–spatial variation index constructed based on the 3-D wavelet textures [44]. The multi-index features are learned via the multikernel SVM [35] since it is able to weight the multiple indexes adaptively, according to their relative importance for a specific task.

The comparison shown in Table XII is very promising as the relearning methods significantly outperform the advanced spectral–spatial classification algorithms. For instance, the accuracy improvements achieved by the relearning methods are about 4% (QuickBird) and 7% (WV-2) when compared with the OBIA approach, which has been proved to be very efficient in HSR image classification. In addition, by comparing Tables VII and XII, it can be found that the filtering and MRF methods do not yield comparable accuracy values to the spectral–spatial classification in the QuickBird experiment, but they give better results in the WV-2 data set.

With respect to the SAR experiments, the CPP algorithms presented in this paper also show obvious advantages for classification. For instance, in the case of the EMISAR experiment, all the CPP algorithms give higher classification accuracy values than the supervised graph embedding algorithm, OA $= 95.6\%$ [39], which was specifically proposed for PolSAR image classification.

VI. CONCLUSION

Most of the current remote sensing image classification algorithms focus on preprocessing techniques, such as dimensionality reduction for hyperspectral imagery [48], spatial feature extraction for HSR imagery [5], and textural feature extraction for SAR data [49]. In general, the basic principle of classification preprocessing is to enhance the spectral feature space by extracting additional discriminative information from the raw spectral bands, in order to improve the classification accuracy. These methods have achieved great success in recent years and are gradually becoming the standard methods for image interpretation. Under this background, in this study, we have presented several new methods for CPP, a strategy that, comparatively, has not received as much attention as classification preprocessing. CPP aims at optimizing or relearning the labeling that is derived from the initial classification, according to some implicit rules related with the spatial arrangement of image primitives in geospatial environments.

It should be underlined that postprocessing has been available for improving remote sensing image classification for a long time, such as the widely used majority filtering. However, it has not received enough attention because researchers regarded it as a marginal method for classification that had limited ability to significantly improve accuracy. In this context, the motivation behind this paper is to update the definition of CPP and to show that CPP strategies are capable of yielding comparable accuracy to the one obtained by advanced spectral–spatial classifiers.

Specifically, we have defined a CPP framework and categorized it into four groups according to the current remote sensing image processing techniques: filtering, object-based approaches, random field, and machine learning. In addition to existing methods, a series of new and effective CPP algorithms have been proposed in this study (see Table I). The proposed CPP framework has been validated using a set of multisource remote sensing data sets, including hyperspectral, HSR, and SAR images.

Our systematic study revealed that CPP algorithms can all smooth the raw classification, reduce the salt-and-pepper effect, and improve accuracy. However, the experimental results indicate that only the newly developed relearning methods are able to enhance discriminative ability and significantly increase classification accuracy. The superiority of the relearning methods can be attributed to the consideration of the occurrence and spatial arrangement of the classes in neighborhoods.

According to the performances presented in the experiments, the following CPP algorithms are suggested: bilateral filter, anisotropic diffusion, random field, and relearning methods. In particular, the proposed relearning strategy, both relearning-Hist and relearning-PCM algorithms, should be included as the baseline of the standard classification methods, due to its convenient implementation and promising classification accuracy.

ACKNOWLEDGMENT

The authors would like to thank the anonymous reviewers for their insightful suggestions, which significantly improved the quality of this paper.

REFERENCES

[1] D. K. McIver and M. A. Friedl, "Using prior probabilities in decision-tree classification of remotely sensed data," *Remote Sens. Environ.*, vol. 81, no. 2/3, pp. 253–261, Aug. 2002.

[2] N. Keshava and J. F. Mustard, "Spectral unmixing," *IEEE Signal Process. Mag.*, vol. 19, no. 1, pp. 44–57, Jan. 2002.

[3] M. Pal and P. M. Mather, "An assessment of the effectiveness of decision tree methods for land cover classification," *Remote Sens. Environ.*, vol. 86, no. 4, pp. 554–565, Aug. 2003.

[4] L. Luo and G. Mountrakis, "Integrating intermediate inputs from partially classified images within a hybrid classification framework: An impervious surface estimation example," *Remote Sens. Environ.*, vol. 114, no. 6, pp. 1220–1229, Jun. 2010.

[5] X. Huang, L. Zhang, and P. Li, "Classification and extraction of spatial features in urban areas using high-resolution multispectral imagery," *IEEE Geosci. Remote Sens. Lett.*, vol. 4, no. 2, pp. 260–264, Apr. 2007.

[6] B. Gong, J. Im, and G. Mountrakis, "An artificial immune network approach to multi-sensor land use/land cover classification," *Remote Sens. Environ.*, vol. 115, no. 2, pp. 600–614, Feb. 2011.

[7] S. W. Myint, P. Gober, A. Brazel, S. Grossman-Clarke, and Q. Weng, "Per-pixel vs. object-based classification of urban land cover extraction using high spatial resolution imagery," *Remote Sens. Environ.*, vol. 115, no. 5, pp. 1145–1161, May 2011.

[8] X. Huang and L. Zhang, "An SVM ensemble approach combining spectral, structural, and semantic features for the classification of high-resolution remotely sensed imagery," *IEEE Trans. Geosci. Remote Sens.*, vol. 51, no. 1, pp. 257–272, Jan. 2013.

[9] S. W. Myint, N. S. N. Lam, and J. Tyler, "Wavelets for urban spatial feature discrimination: Comparisons with fractal, spatial autocorrelation, and spatial co-occurrence approaches," *Photogramm. Eng. Remote Sens.*, vol. 70, no. 7, pp. 803–812, Jul. 2004.

[10] F. Pacifici, M. Chini, and W. J. Emery, "A neural network approach using multi-scale textural metrics from very high-resolution panchromatic imagery for urban land-use classification," *Remote Sens. Environ.*, vol. 113, no. 6, pp. 1276–1292, Jun. 2009.

[11] M. Fauvel, J. Chanussot, and J. A. Benediktsson, "A spatial–spectral kernel-based approach for the classification of remote-sensing images," *Pattern Recognit.*, vol. 45, no. 1, pp. 381–392, Jan. 2012.

[12] X. Huang and L. Zhang, "An adaptive mean-shift analysis approach for object extraction and classification from urban hyperspectral imagery," *IEEE Trans. Geosci. Remote Sens.*, vol. 46, no. 12, pp. 4173–4185, Dec. 2008.

[13] R. Mathieu, C. Freeman, and J. Aryal, "Mapping private gardens in urban areas using object-oriented techniques and very high-resolution satellite imagery," *Landscape Urban Plann.*, vol. 81, no. 3, pp. 179–192, Jun. 2007.

[14] R. Pu and S. Landry, "A comparative analysis of high spatial resolution IKONOS and WorldView-2 imagery for mapping urban tree species," *Remote Sens. Environ.*, vol. 124, pp. 516–533, Sep. 2012.

[15] G. Chirici, D. Giuliarelli, D. Biscontini, D. Tonti, W. Mattioli, M. Marchetti, and P. Corona, "Large-scale monitoring of coppice forest clearcuts by multitemporal very high resolution satellite imagery. A case stud from central Italy," *Remote Sens. Environ.*, vol. 115, no. 4, pp. 1025–1033, Apr. 2011.

[16] W. Zhou, G. Huang, A. Troy, and M. L. Cadenasso, "Object-based land cover classification of shaded areas in high spatial resolution imagery of urban areas: A comparison study," *Remote Sens. Environ.*, vol. 113, no. 8, pp. 1769–1777, Aug. 2009.

[17] J. Stuckens, P. R. Coppin, and M. E. Bauer, "Integrating contextual information with per-pixel classification for improved land cover classification," *Remote Sens. Environ.*, vol. 71, no. 3, pp. 282–296, Mar. 2000.

[18] K. Schindler, "An overview and comparison of smooth labeling methods for land-cover classification," *IEEE Trans. Geosci. Remote Sens.*, vol. 50, no. 11, pp. 4534–4545, Nov. 2012.

[19] S. Geman and D. Geman, "Stochastic relaxation, Gibbs distributions, and the Bayesian restoration of images," *IEEE Trans. Pattern Anal. Mach. Intell.*, vol. PAMI-6, no. 6, pp. 721–741, Nov. 1984.

[20] B. Solaiman, R. K. Koffi, M.-C. Mouchot, and A. Hillion, "An information fusion method for multispectral image classification postprocessing," *IEEE Trans. Geosci. Remote Sens.*, vol. 36, no. 2, pp. 395–406, Mar. 1998.

[21] B. Rodriguez-Cuenca, J. A. Malpica, and M. C. Alonsa, "A spatial contextual postclassification method for preserving linear objects in multispectral imagery," *IEEE Trans. Geosci. Remote Sens.*, vol. 51, no. 1, pp. 174–183, Jan. 2013.

[22] T. Van de Voorde, W. De Genst, and F. Canters, "Improving pixel-based VHR land-cover classifications of urban areas with post-classification techniques," *Photogramm. Eng. Remote Sens.*, vol. 73, no. 9, pp. 1017–1027, Sep. 2003.

[23] P. Perona and J. Malik, "Scale-space and edge detection using anisotropic diffusion," *IEEE Trans. Pattern Anal. Mach. Intell.*, vol. 12, no. 7, pp. 629–639, Jul. 1990.

[24] C. Tomasi and R. Manduchi, "Bilateral filtering for gray and color images," in *Proc. 6th IEEE Int. Conf. Comput. Vis.*, Bombay, India, 1998, pp. 839–846.

[25] T. Blaschke, "Object based image analysis for remote sensing," *Proc. ISPRS Int. J. Photogramm. Remote Sens.*, vol. 65, no. 1, pp. 2–16, Jan. 2010.

[26] S. van der Linder, A. Janz, B. Waske, M. Eiden, and P. Hostert, "Classifying segmented hyperspectral data from a heterogeneous urban environment using support vector machines," *J. Appl. Remote Sens.*, vol. 1, no. 1, p. 013543, Oct. 2007.

[27] Y. Tarabalka, J. Chanussot, and J. A. Benediktsson, "Spectral–spatial classification of hyperspectral imagery based on partitional clustering techniques," *IEEE Trans. Geosci. Remote Sens.*, vol. 47, no. 8, pp. 2973–2987, Aug. 2009.

[28] S. Aksoy, I. Z. Yalniz, and K. Tasdemir, "Automatic detection and segmentation of orchards using very high resolution imagery," *IEEE Trans. Geosci. Remote Sens.*, vol. 50, no. 8, pp. 3117–3131, Aug. 2012.

[29] G. Moser, S. B. Serpico, and J. A. Benediktsson, "Land-cover mapping by Markov modeling of spatial-contextual information in very-high-resolution remote sensing images," *Proc. IEEE*, vol. 101, no. 3, pp. 631–651, Mar. 2013.

[30] S. Z. Li, *Markov Random Field Modeling in Image Analysis*. New York, NY, USA: Springer-Verlag, 2010.

[31] Y. Boykov, O. Veksler, and R. Zabih, "Fast approximate energy minimization via graph cuts," *IEEE Trans. Pattern Anal. Mach. Intell.*, vol. 23, no. 11, pp. 1222–1239, Nov. 2001.

[32] R. M. Haralick, K. Shanmugam, and I. Dinstein, "Textural features for image classification," *IEEE Trans. Syst., Man Cybern.*, vol. SMC-3, no. 6, pp. 610–621, Nov. 1973.

[33] X. Huang, L. Zhang, and P. Li, "An adaptive multiscale information fusion approach for feature extraction and classification of IKONOS

multispectral imagery over urban areas," *IEEE Geosci. Remote Sens. Lett.*, vol. 4, no. 4, pp. 654–658, Oct. 2007.
[34] D. Barash and D. Comaniciu, "A common framework for nonlinear diffusion, adaptive smoothing, bilateral filtering and mean shift," *Image Vis. Comput.*, vol. 22, no. 1, pp. 73–81, Jan. 2004.
[35] D. Tuia, G. Camps-Valls, G. Matasci, and M. Kanevski, "Learning relevant image features with multiple-kernel classification," *IEEE Trans. Geosci. Remote Sens.*, vol. 48, no. 10, pp. 3780–3791, Oct. 2010.
[36] D. A. Landgrebe, *Signal Theory Methods in Multispectral Remote Sensing*. Hoboken, NJ, USA: Wiley, 2003.
[37] J. S. Lee, M. R. Grunes, and E. Pottier, "Quantitative comparison of classification capability: Fully-polarimetric versus dual and single-polarization SAR," *IEEE Trans. Geosci. Remote Sens.*, vol. 39, no. 11, pp. 2343–2351, Nov. 2001.
[38] G. M. Foody, "Thematic map comparison: Evaluating the statistical significance of differences in classification accuracy," *Photogramm. Eng. Remote Sens.*, vol. 70, no. 5, pp. 627–633, May 2004.
[39] L. Shi, L. Zhang, J. Yang, L. Zhang, and P. Li, "Supervised graph embedding for polarimetric SAR image classification," *IEEE Geosci. Remote Sens. Lett.*, vol. 10, no. 2, pp. 216–220, Mar. 2013.
[40] M. Fauvel, Y. Tarabalka, J. A. Benediktsson, J. Chanussot, and J. Tilton, "Advances in spectral–spatial classification of hyperspectral images," *Proc. IEEE*, vol. 101, no. 3, pp. 652–675, Mar. 2013.
[41] R. L. Kettig and D. A. Landgrebe, "Classification of multispectral image data by extraction and classification of homogeneous objects," *IEEE Trans. Geosci. Electron.*, vol. GE-14, no. 1, pp. 19–26, Jan. 1976.
[42] A. B. Santos, A. de. A. Araujo, and D. Menotti, "Combining multiple classification methods for hyperspectral data interpretation," *IEEE J. Sel. Topics Appl. Earth Observ. Remote Sens.*, vol. 6, no. 3, pp. 1450–1459, Jun. 2013.
[43] M. Pesaresi and J. A. Benediktsson, "A new approach for the morphological segmentation of high-resolution satellite imagery," *IEEE Trans. Geosci. Remote Sens.*, vol. 39, no. 2, pp. 309–320, Feb. 2001.
[44] H. Y. Yoo, K. Lee, and B. D. Kwon, "Quantitative indices based on 3D discrete wavelet transform for urban complexity estimation using remotely sensed imagery," *Int. J. Remote Sens.*, vol. 30, no. 23, pp. 6219–6239, 2009.
[45] X. Huang and L. Zhang, "Comparison of vector stacking, multi-SVMs fuzzy output, and multi-SVMs voting methods for multiscale VHR urban mapping," *IEEE Geosci. Remote Sens. Lett.*, vol. 7, no. 2, pp. 261–265, Apr. 2010.
[46] X. Huang, Q. Lu, and L. Zhang, "A multi-index learning approach for classification of high-resolution remotely sensed images over urban areas," *ISPRS J. Photogramm. Remote Sens.*, vol. 90, pp. 36–48, Apr. 2014.
[47] X. Huang and L. Zhang, "Morphological building/shadow index for building extraction from high-resolution imagery over urban areas," *IEEE J. Sel. Topics Appl. Earth Observ. Remote Sens.*, vol. 5, no. 1, pp. 161–172, Feb. 2012.
[48] A. Plaza, P. Martinez, J. Plaza, and R. Perez, "Dimensionality reduction and classification of hyperspectral image data using sequences of extended morphological transformations," *IEEE Trans. Geosci. Remote Sens.*, vol. 43, no. 3, pp. 466–479, Mar. 2005.
[49] S. Fukuda and H. Hirosawa, "A wavelet-based texture feature set applied to classification of multifrequency polarimetric SAR images," *IEEE Trans. Geosci. Remote Sens.*, vol. 37, no. 5, pp. 2282–2286, Sep. 1999.

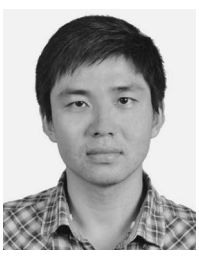

Xin Huang (M'13) received the Ph.D. degree in photogrammetry and remote sensing from the State Key Laboratory of Information Engineering in Surveying, Mapping and Remote Sensing (LIESMARS), Wuhan University, Wuhan, China, in 2009.

He is currently a Full Professor with the LIESMARS. He has published more than 40 peer-reviewed articles in international journals. He has frequently served as a referee for many international journals for remote sensing. His research interests include hyperspectral data analysis, high-resolution image processing, pattern recognition, and remote sensing applications.

Dr. Huang was the recipient of the Top-Ten Academic Star of Wuhan University in 2009, the Boeing Award for best paper in image analysis and interpretation from the American Society for Photogrammetry and Remote Sensing in 2010, the New Century Excellent Talents in University from the Ministry of Education of China in 2011, and the National Excellent Doctoral Dissertation Award of China in 2012. In 2011, he was also recognized by the IEEE Geoscience and Remote Sensing Society as a Best Reviewer of the IEEE GEOSCIENCE AND REMOTE SENSING LETTERS.

Qikai Lu received the B.S. and M.S. degrees from Wuhan University, Wuhan, China, in 2011 and 2013, respectively. He is currently working toward the Ph.D. degree in photogrammetry and remote sensing.

He is currently with the State Key Laboratory of Information Engineering in Surveying, Mapping, and Remote Sensing, Wuhan University. His research interests include image processing, machine learning, and remote sensing applications.

Liangpei Zhang (M'06–SM'08) received the B.S. degree in physics from Hunan Normal University, Changsha, China, in 1982; the M.S. degree in optics from the Chinese Academy of Sciences, Xian, China, in 1988; and the Ph.D. degree in photogrammetry and remote sensing from Wuhan University, Wuhan, China, in 1998.

He is currently the Head of the Remote Sensing Division, State Key Laboratory of Information Engineering in Surveying, Mapping and Remote Sensing, Wuhan University. He is also a Chang-Jiang Scholar Chair Professor appointed by the Ministry of Education of China. He is currently a Principal Scientist for the China State Key Basic Research Project (2011–2016) appointed by the Ministry of National Science and Technology of China to lead the remote sensing program in China. He has more than 300 research papers. He is the holder of five patents. His research interests include hyperspectral remote sensing, high-resolution remote sensing, image processing, and artificial intelligence.

Dr. Zhang is a Fellow of the Institution of Engineering and Technology, an Executive Member (Board of Governor) of the China National Committee of the International Geosphere-Biosphere Programme, and an Executive Member of the China Society of Image and Graphics. He regularly serves as a Cochair of the series SPIE Conferences on Multispectral Image Processing and Pattern Recognition, Conference on Asia Remote Sensing, and many other conferences. He edits several conference proceedings, issues, and Geoinformatics symposiums. He also serves as an Associate Editor of the *International Journal of Ambient Computing and Intelligence*, the *International Journal of Image and Graphics*, the *International Journal of Digital Multimedia Broadcasting*, the *Journal of Geo-spatial Information Science*, the *Journal of Remote Sensing*, and the IEEE TRANSACTIONS ON GEOSCIENCE AND REMOTE SENSING.

Antonio Plaza (M'05–SM'07) received the M.S. and Ph.D. degrees in computer engineering from the University of Extremadura, Caceres, Spain.

He is an Associate Professor (with accreditation for Full Professor) with the Department of Technology of Computers and Communications, University of Extremadura, where he is the Head of the Hyperspectral Computing Laboratory (HyperComp). He was elevated to IEEE Senior Member status in 2007. He was the Coordinator of the Hyperspectral Imaging Network, a European project with total funding of 2.8 million Euro. He authored more than 400 publications, including more than 110 JCR journal papers (66 in IEEE journals), 20 book chapters, and over 240 peer-reviewed conference proceeding papers (94 in IEEE conferences). He has guest edited seven special issues on JCR journals (three in IEEE journals).

Dr. Plaza has been a Chair for the IEEE Workshop on Hyperspectral Image and Signal Processing: Evolution in Remote Sensing (2011). He was a recipient of the recognition of Best Reviewers of the IEEE GEOSCIENCE AND REMOTE SENSING LETTERS (2009) and the IEEE TRANSACTIONS ON GEOSCIENCE AND REMOTE SENSING (2010), a journal for which he has served as an Associate Editor during 2007–2012. He is also an Associate Editor for the IEEE ACCESS and the IEEE GEOSCIENCE AND REMOTE SENSING MAGAZINE and was a member of the Editorial Board of the IEEE GEOSCIENCE AND REMOTE SENSING NEWSLETTER (2011–2012) and of the steering committee of the IEEE JOURNAL OF SELECTED TOPICS IN APPLIED EARTH OBSERVATIONS AND REMOTE SENSING (2012). He served as the Director of Education Activities for the IEEE Geoscience and Remote Sensing Society (GRSS) during 2011–2012. He has been serving as President of the Spanish Chapter of the IEEE GRSS since November 2012 and as Editor-in-Chief of the IEEE TRANSACTIONS ON GEOSCIENCE AND REMOTE SENSING journal since January 2013.